The Astronomical Journal, 149:117 (17pp), 2015 April doi:10.1088/0004-6256/149/4/117

LARGE MAGELLANIC CLOUD NEAR-INFRARED SYNOPTIC SURVEY. I. CEPHEID VARIABLES AND THE CALIBRATION OF THE LEAVITT LAW

Lucas M. Macri[1], Chow-Choong Ngeow[2], Shashi M. Kanbur[3], Salma Mahzooni[1], and Michael T. Smitka[1]
[1] Mitchell Institute for Fundamental Physics & Astronomy, Department of Physics & Astronomy, Texas A&M University, College Station, TX 77843, USA; lmacri@tamu.edu
[2] Graduate Institute of Astronomy, National Central University, Jhongli 32001, Taiwan
[3] Department of Physics, The State University of New York at Oswego, Oswego, NY 13126, USA
Received 2014 August 10; accepted 2014 November 26; published 2015 March 4

ABSTRACT

We present observational details and first results of a near-infrared (JHK_s) synoptic survey of the central region of the Large Magellanic Cloud (LMC) using the CPAPIR camera at the CTIO 1.5 m telescope. We covered 18 square degrees to a depth of $K_s \sim 16.5$ mag and obtained an average of 16 epochs in each band at any given location. Our catalog contains more than 3.5×10^6 sources, including 1417 Cepheid variables previously studied at optical wavelengths by the OGLE survey. Our sample of fundamental-mode pulsators represents a nine-fold increase in the number of these variables with time-resolved, multi-band near-infrared photometry. We combine our large Cepheid sample and a recent precise determination of the distance to the LMC to derive a robust absolute calibration of the near-infrared Leavitt Law for fundamental-mode and first-overtone Cepheids with 10× better constraints on the slopes relative to previous work. We also obtain calibrations for the tip of the red giant branch and the red clump based on our ensemble photometry which are in good agreement with previous determinations.

Key words: distance scale – Magellanic Clouds – stars: variables: Cepheids

Supporting material: machine-readable and VO tables

1. INTRODUCTION

The Cepheid period–luminosity relation (Leavitt & Pickering 1912, hereafter "The Leavitt Law") is one of the cornerstones of the extragalactic distance scale. It has been widely used over the past century, from Hubble's proof of the extragalactic nature of "spiral nebulae" (Hubble 1925) to the most accurate and precise local determination of the Hubble constant (H_0) to date (Riess et al. 2011). Increasingly more precise and accurate determinations of H_0 provide needed additional constraints on the equation of state of dark energy and other important cosmological parameters (Weinberg et al. 2013). In order to achieve these goals, further improvements in the characterization of the Leavitt Law are required. These include a more robust zeropoint calibration, better constraints on variations of zeropoint and slope as a function of metallicity, and stronger limits on nonlinearity.

The first generation of microlensing surveys directed toward the LMC resulted in the discovery of thousands of Cepheid variables (Alcock 1999; Udalski et al. 1999 from the MACHO and OGLE surveys respectively). At optical wavelengths, many studies have been carried out using the Cepheid photometry obtained by the OGLE survey, which provides excellent phase coverage in the standard *BVI* bands (e.g., Ngeow & Kanbur 2005; Bono et al. 2010). At near-infrared wavelengths, the observational material available to date is more limited. Both 2MASS (Skrutskie et al. 2006) and the IRSF Magellanic Clouds Point Source Catalog (Kato et al. 2007) provide complete coverage of the galaxy in JHK_s but are limited to a single epoch, requiring corrections to mean light (Nikolaev et al. 2004; Soszyński et al. 2005). Synoptic observations are either limited to a single band (K_s for the VMC, Cioni et al. 2011; Ripepi et al. 2012) or to a relatively small number of variables compared to the optical samples ($N = 92$, Persson et al. 2004, hereafter P04).

Recently, Pietrzyński et al. (2013) obtained a very accurate and precise determination of the distance to the LMC through the discovery and analysis of detached eclipsing binary systems, $D = 49.97 \pm 2\%$ kpc (equivalent to a distance modulus of $\mu_0 = 18.493 \pm 0.048$ mag). Such a robust distance estimate makes the LMC a very important component in the "first rung" of the extragalactic distance scale by enabling absolute calibrations of many distance indicators, such as Cepheids.

Motivated by the above, we carried out a synoptic multi-wavelength near-infrared survey of the central region of the LMC that has yielded well-sampled light curves for 1417 Cepheids and an additional 3.5×10^6 sources. This paper, the first in a series, presents details of the observations, data reduction and photometry (Section 2) and the resulting Cepheid light curves and Leavitt Law (Section 3). Future work will include a Fourier analysis of Cepheid light curve structure (Bhardwajj et al. 2014), a study of nonlinearity in the Leavitt Law and P–L relations of long-period variables, among other topics.

2. OBSERVATIONS, DATA REDUCTION, PHOTOMETRY, AND CALIBRATION

2.1. Observations and Data Reduction

Images were acquired using the CPAPIR camera (Artigau et al. 2004) at the 1.5 m telescope of the Cerro Tololo Inter-American Observatory, operated by the SMARTS consortium. CPAPIR uses a 2048 × 2048 Hawaii-2 infrared array detector and delivers an effective plate scale at this telescope of 0.″983 pixel^{-1}, or a field of view of 0.°559 on a side. We requested observations centered on 49 different positions, with extensive overlap among neighboring fields to enable a robust photometric cross-calibration. Figure 1 shows the area covered by the

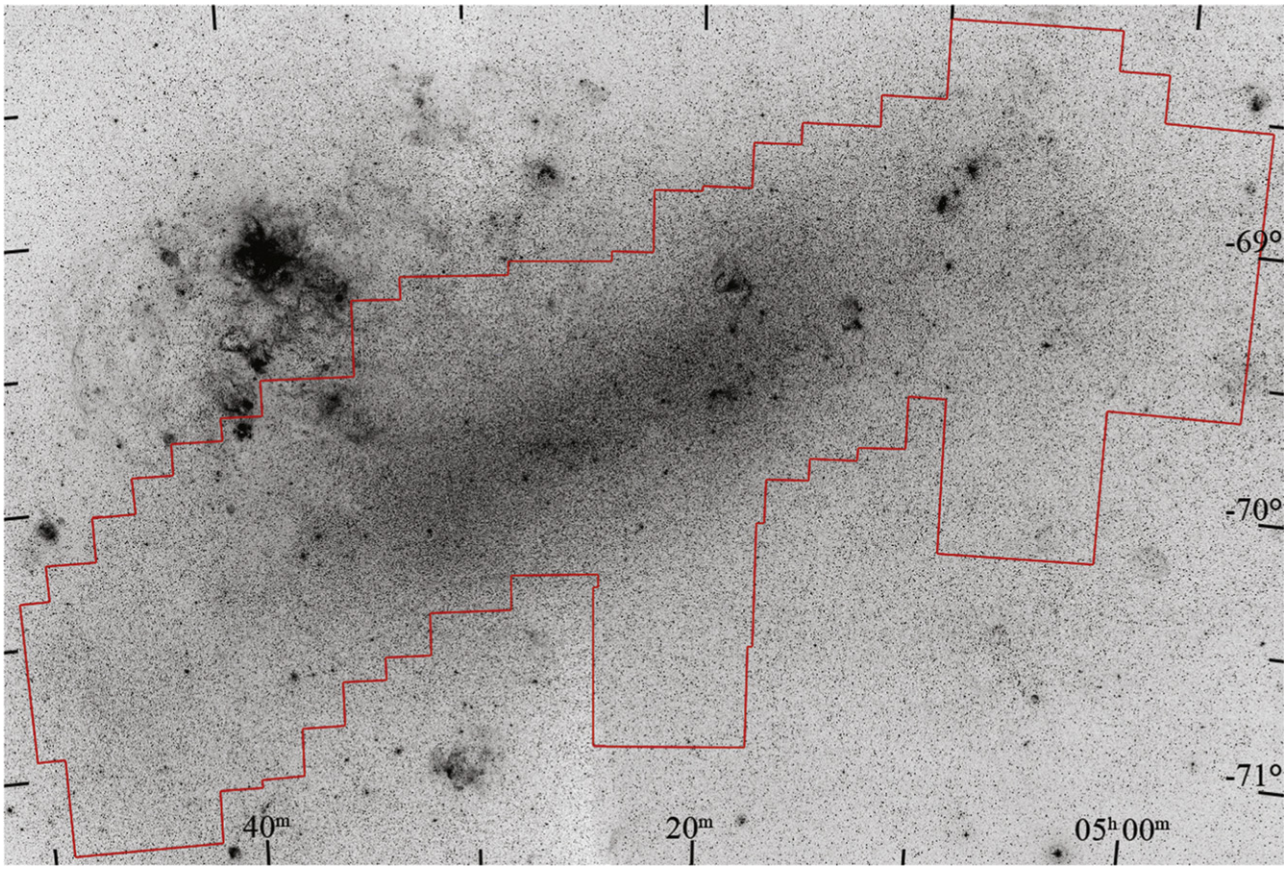

Figure 1. Digitized Sky Survey image of the Large Magellanic Cloud showing the area covered by our CPAPIR observations (red outline), which amounts to 18 square degrees.

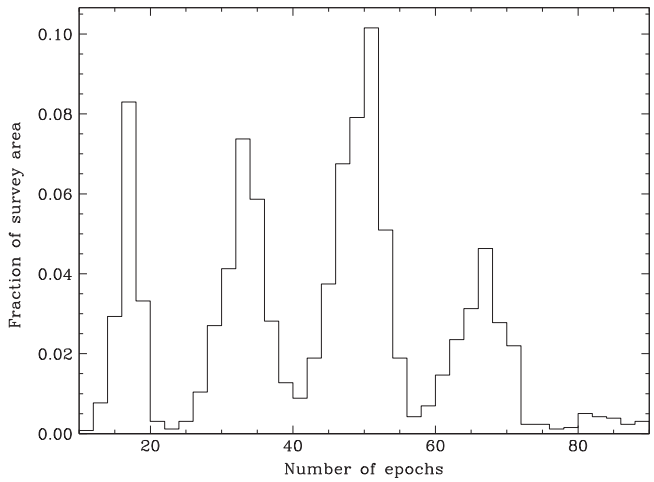

Figure 2. Histogram of the fraction of the survey area that was imaged on a given number of epochs. The peak near 16 epochs corresponds to areas that do not overlap with neighboring fields.

observations, which amounts to slightly over 18 square degrees.

Observations were obtained in queue mode on 32 separate nights during three distinct time periods: 2006 November (7 nights), 2007 January (6 nights), and 2007 November (19 nights). Individual fields were targeted on 7–11 nights, often twice on each night, so that every location within our survey area was observed on 14–20 distinct epochs. Given the significant overlap between fields, many locations within our survey area were imaged on 2–4× as many epochs (see Figure 2). Each unit of imaging consisted of a six-point dither (2×3 in R.A. and decl., respectively) with commanded steps of $10''$ in each direction. A single 10s exposure was obtained at each dither point for the J and H sequences, while a 2×5s coadd was executed for the K_s sequence. Calibration images (darks and dome flats in J and H) were obtained nightly.

Images were processed using the IRAF[4] packages `XDIMSUM` and `CCDRED`. The reduction steps consisted of bad-pixel masking (based on the median dark frame), dark current subtraction, and flat-fielding. We used dome flats for J and H and sky flats for K_s. The latter were generated by median-combining all the science images obtained on a given night, after masking all $>3\sigma$ sources present on each image. This step was performed using the `xslm` routine and was repeated twice to ensure all the significant sources were masked, using the first-pass masked images for the second iteration. The reduced data set consists of 19,604 scientifically useful images, which are available upon request.

2.2. PSF Photometry and Relative Calibration

We performed time-series photometry of the reduced images using `DAOPHOT/ALLSTAR` (Stetson 1987) and `ALLFRAME` (Stetson 1994), as well as supporting programs kindly

[4] IRAF is distributed by the National Optical Astronomy Observatory, which is operated by the Association of Universities for Research in Astronomy (AURA) under cooperative agreement with the National Science Foundation.

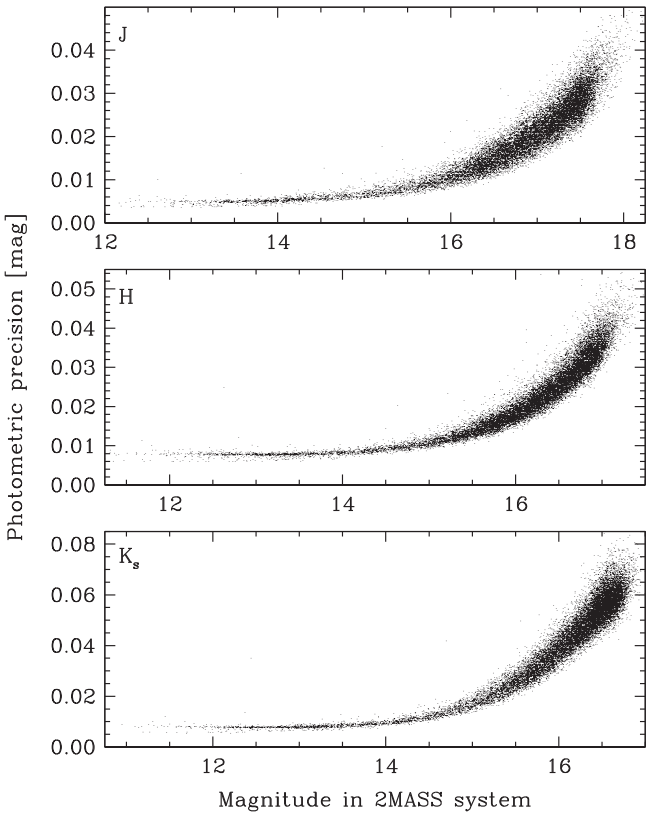

Figure 3. Internal photometric precision of our observations as a function of magnitude for the J (top), H (center), and K_s (bottom) bands for one representative field. We selected stars with three-band photometry, Stetson variability index $J \leqslant 0.5$ in all bands, and located within 1000 pixels in radius of the field center.

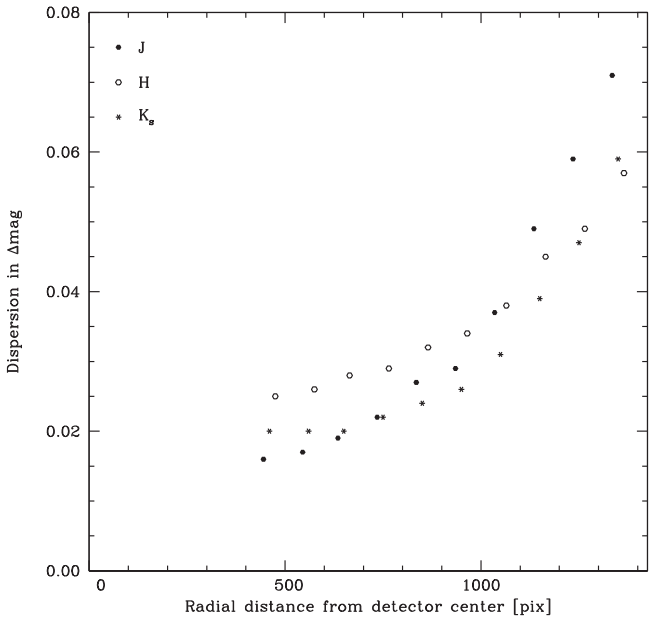

Figure 4. Test of our external photometric calibration uncertainty as a function of radial distance from detector center for the J (filled circles), H (open circles), and K_s (stars) bands. The lack of measurements at radial distances below 400 pixels is due to the fact that even the most overlapping fields were offset by at least 1/4 of the detector width. Note the rapid degradation of photometric accuracy toward the corners of the detector.

provided by P. Stetson. We performed the steps described below for each combination of field and filter (i.e., 49×3 separate reductions).

We first identified all $>5\sigma$ sources present in each image and obtained aperture photometry with a radius of 5 pixels, with a sky annulus extending from 5 to 8 pixels. We then selected up to 200 bright and isolated stars in each image to determine its point-spread function, which was modeled as a Gaussian or a Moffat profile with no spatial variation, and performed PSF photometry of all the sources detected in the first step. We used this photometry to derive accurate frame-to-frame coordinate transformations using DAOMATCH and DAOMASTER (Stetson 1993). We found the typical displacement of the initial central position at each epoch to be comparable to the dither pattern (i.e., 20–30″ or ∼1% of the field width).

Next, we used Stetson's MONTAGE program to select the 50 highest-quality images (using a metric based on the FWHM of the PSF and the flux level of each image) and median-combined them into a higher signal-to-noise ratio reference frame. We repeated the steps described in the previous paragraph for the reference frame and used the resulting star list as input for the ALLFRAME PSF photometry run. Once this was completed, we determined a position-dependent magnitude correction for each image, relative to the photometry of the frame with the highest value of the quality metric, as follows. We used ∼1000 bright stars distributed throughout the field to calculate the mean magnitude offset as a function of position, carrying out the calculation every 45 pixels in x and y based on stars within ±180 pixels, and fit a thin-plate spline to the resulting values. We applied the magnitude correction by evaluating the spline fit at the position of each star. This procedure was very effective at removing low-frequency spatial variations in the photometric zeropoint, specially near the edges of the field where the optical distortion of the camera is more pronounced. As an example, the J-band images of field 1 typically exhibited zeropoint variations of 0.08 and 0.22 mag (50% and 90% widths of the distribution, respectively) before the correction and 0.02 and 0.06 mag after the correction. Next, we used Stetson's TRIAL program to extract light curves and to calculate mean instrumental magnitudes and variability indices ($J_{\rm Stet}$, Stetson 1996). Figure 3 shows our internal photometric precision as a function of magnitude in each of the three bands, for stars without any discernible intrinsic variability.

2.3. Calibration to the 2MASS System

Once the preceding steps were completed, we matched and merged the final J, H and K_s star catalogs of each field using DAOMATCH and DAOMASTER and carried out the final astrometric and photometric calibrations using the 2MASS Point Source Catalog (Cutri et al. 2003b) as reference. The calibrations were derived and applied separately for each of the 49 fields. Regions in common between neighboring fields were later used to test the quality of these calibration procedures.

We performed the astrometric calibration using WCSTools (Mink 2002), based on 600–900 bright stars in common between 2MASS and the star catalog of a given field. Once a solution was determined and applied for a given field, we matched its full photometric catalog against 2MASS with a radial tolerance of 1″ and found $6–14 \times 10^3$ stars in common. Based on the distribution of the residuals, we determined an

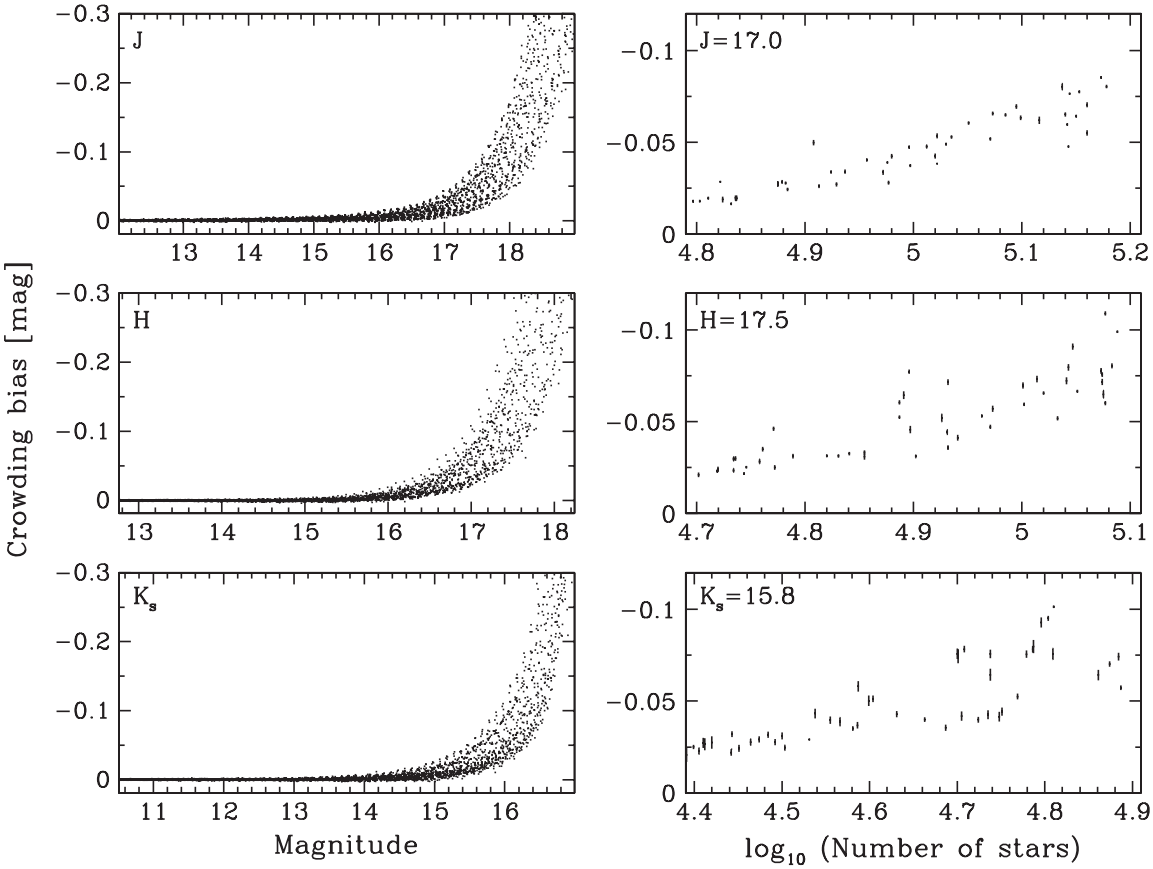

Figure 5. Results of the artificial star simulations to characterize photometric bias due to crowding. Left: bias vs. magnitude for each of the 49 fields. Right: the spread in bias at a given magnitude is well correlated with the total stellar density of the field.

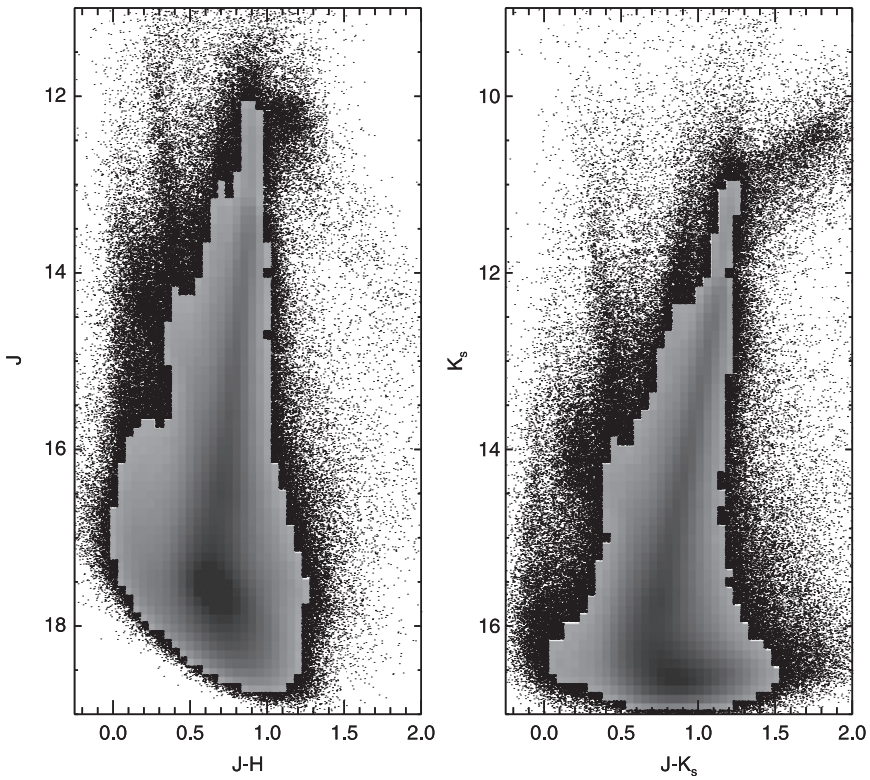

Figure 6. Color–magnitude/Hess diagrams based on $\sim 3.6 \times 10^6$ (left) and 2×10^6 (right) stars with a minimum of two-band photometry. The Hess diagram is used in areas where the stellar density exceeds 200 objects per bin.

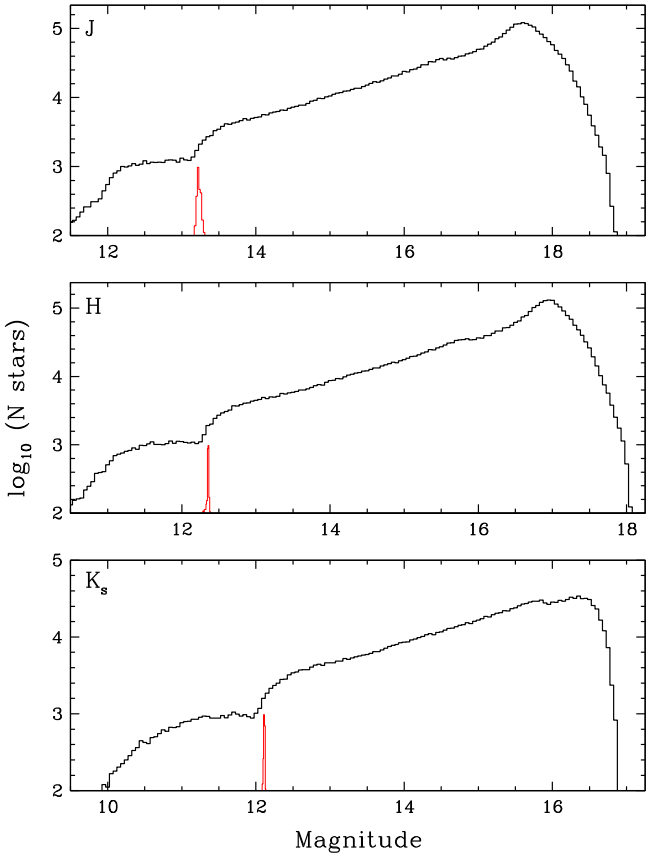

Figure 7. Differential luminosity functions in J (top), H (center), and K_s (bottom) for stars with $J-H>0.4$ (top and center) or $J-K_s>0.5$ (bottom). The histograms plotted in red show the distribution of TRGB magnitudes obtained in 400 realizations of the edge-detection filter algorithm described in Section 3.1.

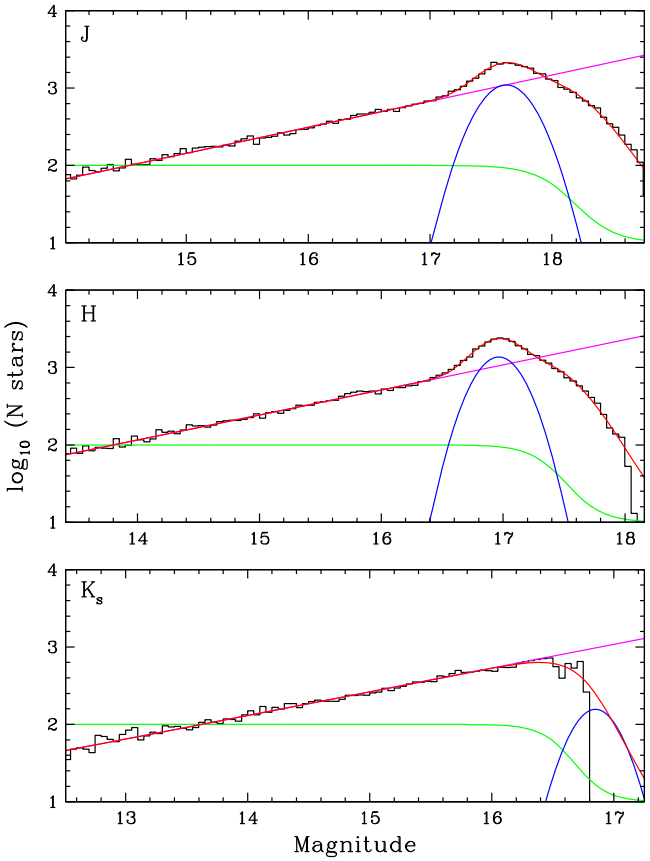

Figure 8. Differential luminosity functions in J (top), H (center), and K_s (bottom) for stars with $0.4<J-H<1.0$ (top and center) or $0.5<J-K_s<1.1$ (bottom), fit using Equation 2. The magenta line represents the power-law component that fits the RGB LF, the blue line indicates the Gaussian component that fits the RC, and the green line shows the photometric incompleteness function $I(m)$ (offset by +1 for plotting purposes). The red line denotes the combination of all components.

astrometric uncertainty of 0.″15 (all uncertainties quoted in this work are 1σ values).

The absolute photometric calibration was carried out using the same type of spline-fitting procedure described in Section 2.2. While that procedure only corrected the spatial variations in the zeropoint of a given frame to the instrumental system of its reference frame, this step corrected the ensemble photometry of each field/filter combination for the spatial variations in the zeropoint of its reference frame. We used $2–8\times10^3$ stars (depending on field and filter) for this correction, limiting the sample to objects with 2MASS magnitudes fainter than 11 (to avoid nonlinearities) and 2MASS photometric uncertainties below 0.1 mag, equivalent to $J\sim16.1$, $H\sim15.2$, and $K_s\sim14.6$ mag (as shown in Figure 3, the CPAPIR internal photometric uncertainties were 5–15× smaller). As in the previous case, the use of a spline-fitting technique was very helpful in decreasing the dispersion in the photometric solution, achieving reductions of a factor of ∼1.5 in J and H and ∼2 in K_s.

We quantified the accuracy of our absolute photometric calibration by identifying objects in common between overlapping fields and calculating the uncertainty in Δmag for stars with the highest internal precision ($J\leqslant15$, $H\leqslant14.5$, $K_s\leqslant14$) as a function of radius from the field center. The results of this comparison are plotted in Figure 4, with the lack of stars at radii below 400 pixels due to the fact that even the most overlapping fields were offset by at least 1/4 of the detector size. It can be seen that our total photometric calibration uncertainty near the center of the detector is only 11, 18, and 14 mmag in JHK_s, respectively, degrading rapidly for stars located at radii beyond the width of the detector. This position-dependent uncertainty has been fully propagated.

Table 1
Result of Fits to the RGB and Red Clump

Parameter	Value		
	J	H	K_s
RGB LF slope (b)	0.34 ± 0.01	0.33 ± 0.01	0.34 ± 0.01
RC width (σ_{RC})	0.17 ± 0.01	0.17 ± 0.01	...
RC mean magnitude[a] (m_{RC})	17.57 ± 0.03	16.91 ± 0.04	...
50% incompl. (m_I)	18.04 ± 0.09	17.39 ± 0.10	16.51 ± 0.05
Inc. scale length (ξ_I)	0.15 ± 0.01	0.12 ± 0.01	0.11 ± 0.01

[a] The quoted values include crowding corrections but have not been corrected for extinction (see Section 3.4).

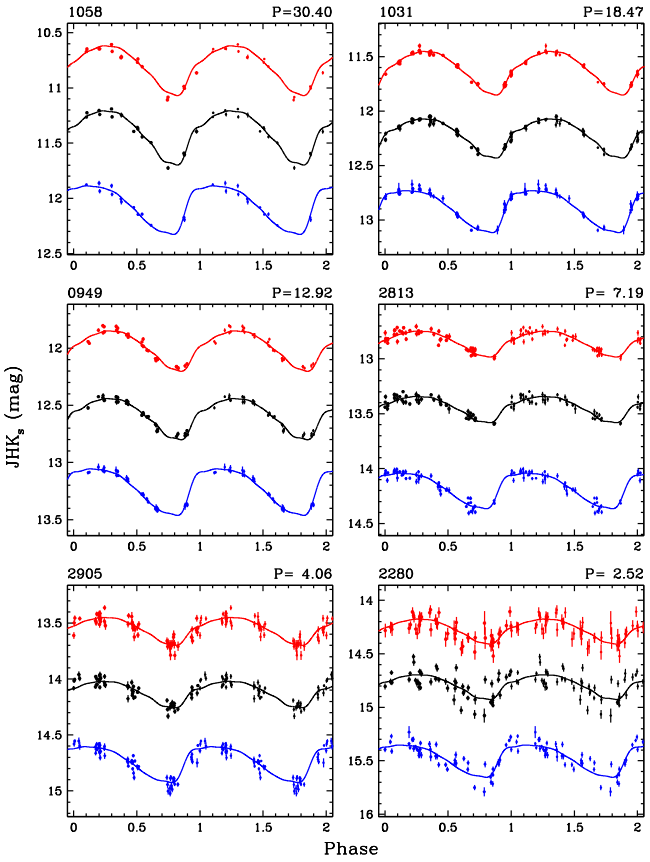

Figure 9. Representative light curves of six fundamental-mode Cepheids spanning the entire range of periods in our sample. The J and K_s light curves (in blue and red, respectively) have been offset for clarity by +0.25 and −0.5 mag. The solid lines represent the best-fit templates from Soszyński et al. (2005).

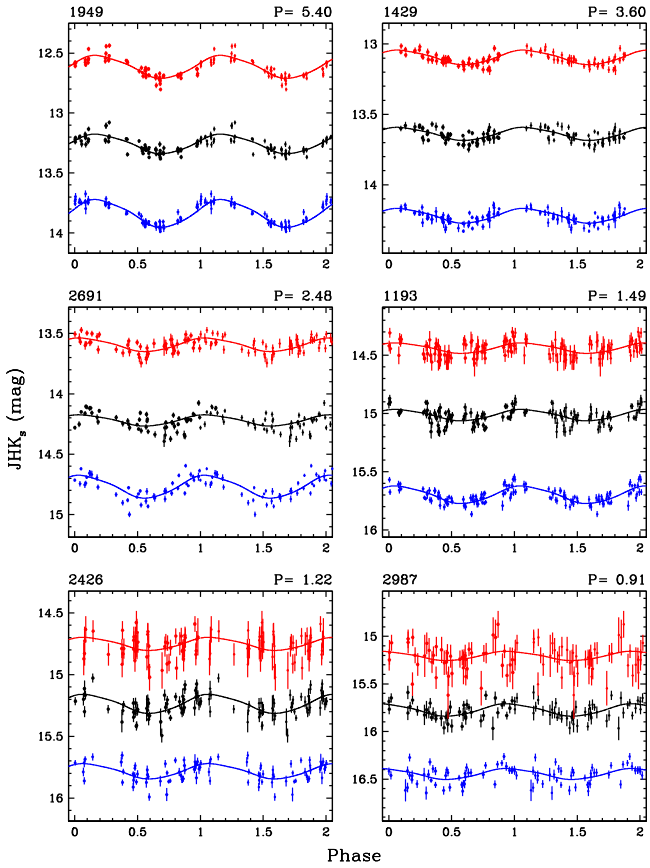

Figure 10. Representative light curves of six first-overtone Cepheids spanning the entire range of periods in our sample. The J and K_s light curves (in blue and red, respectively) have been offset for clarity by +0.25 and −0.5 mag. The solid lines represent the best-fit sinusoidal templates.

As part of our photometric calibration procedure, we also solved for color terms such as

$$J = J' + \xi^{J}_{JK_s}(J - K_s) \quad (1)$$

where J and K_s are the fully calibrated magnitudes in the 2MASS system, J' is the CPAPIR magnitude partially calibrated into the 2MASS system (zeropoint-corrected but not color-term corrected), and $\xi^{J}_{JK_s}$ is the color term for J based on the J–K_s color. This was, in fact, the only statistically significant color term that we determined, with a value of +0.018 ± 0.002.

2.4. Crowding Corrections

Even though our fields do not have a very high density of resolved point sources (6×10^{-3}–4×10^{-2} stars/pixel) we carried out a full suite of simulations to characterize any photometric biases due to crowding. We used the ADDSTAR routine in DAOPHOT to randomly place artificial stars in all master images using their corresponding PSFs, subject to the following constraints: (i) the number of artificial stars that were added was only 5% of the number of actual point sources (so as to not excessively increase the stellar density of each field); (ii) the magnitudes of the artificial stars were obtained by randomly sampling the observed luminosity function; (iii) no artificial star was allowed to fall within 2.5 pixels of any other object (real or artificial) to avoid blends; (iv) the positions of the artificial stars were restricted to the innermost 80% of the detector in x and y, to avoid the PSF distortion near the edges of the field; (v) 20 realizations of each master frame were produced, to increase the statistics.

We carried out photometry of the fake master images using ALLSTAR in the same manner as when we analyzed the original master images, matched the input and output star lists and derived offsets as a function of magnitude. These are shown in the left panels of Figure 5. The spread in crowding bias at the faint end for a given magnitude is well correlated

Table 2
Cepheid Photometry

ID	Band	MJD[a]	Phase[b]	Mag	σ
0473	J	42.6048	0.313	15.132	0.037
0473	J	42.7381	0.364	15.060	0.025
0473	J	45.7243	0.497	15.117	0.017
0473	J	45.8612	0.549	15.213	0.020
0473	J	106.5305	0.587	15.151	0.017

Notes. IDs are from the OGLE-III catalog (Soszyński et al. 2008).
[a] JD-2450000.
[b] Based on P and $T_{I,\max}$ from the OGLE catalogs (Soszyński et al. 2008; Ulaczyk et al. 2013).

(This table is available in its entirety in machine-readable and Virtual Observatory (VO) forms.)

Table 3
Cepheid Properties

ID	P (days)	Cl	Mean Magnitudes					σ			LC Amplitudes			E_{VI}	QF	UF
			V	I	J	H	K_s	J	H	K_s	J	H	K_s			
0473	2.634	FU	16.324	15.588	15.109	14.845	14.624	80	116	116	238	288	283	90	F	N
0474	0.816	FO	17.338	16.535	16.195	15.687	15.579	131	152	171	192	70	60	90	F	N
0477	1.959	FO	16.142	15.456	15.142	14.678	14.607	50	54	64	274	50	9	100	D	Y
0478	2.764	FU	16.155	15.464	14.979	14.654	14.609	56	73	78	344	45	91	110	D	Y
0480	4.035	FU	16.868	15.755	15.119	14.503	14.497	48	52	80	555	489	624	130	D	N

Notes. IDs, periods, and *VI* magnitudes are from the OGLE catalogs (Soszyński et al. 2008; Ulaczyk et al. 2013). Magnitudes are corrected for crowding but not for extinction. E_{VI} values are taken from Haschke et al. (2011). Magnitude uncertainties, light curve amplitudes, and reddenings are expressed in mmag. Cl: class (FUndamental or First Overtone); QF: quality flag (see Table 4); UF: flag to indicate if the variable was used in the final P–L fits. Only the first five lines of the Table are presented here; the rest can be found in the online supplemental material.

(This table is available in its entirety in machine-readable and Virtual Observatory (VO) forms.)

Table 4
Quality Flags for Cepheid Light Curves

Flag	Description	Range	N
		Fundamental Mode	
G	Below minimum period or lacks three-band data	$P < 2.5$	60
F	Exceeds maximum light curve rms	$\sigma(J) > 0.07$, $\sigma(H) > 0.08$, $\sigma(K_s) > 0.09$	71
E	Outlier in color–color relation	$J - K_s = 0.165 + 0.749(J - H)$, $\Delta > 0.13$	18
D	Outlier in NIR amplitude ratios	$H/J = 0.82 + 0.20 \log P$, $\Delta > 0.40$ $K_s/J = 0.80 + 0.26 \log P$, $\Delta > 0.36$ $H/K_s = 1.03 - 0.08 \log P$, $\Delta > 0.52$	77
C	Phase difference of maximum light	$\Delta\phi(I, JHK_s) \notin (-0.025, 0.06)$ for $\log P < 0.85$	44
B	Outlier in NIR-to-I amplitude ratios	$J/I = 0.67 + 0.17 \log P + 0.14(\log P)^2$, $\Delta > 0.23$ $H/I = 0.54 + 0.29 \log P + 0.25(\log P)^2$, $\Delta > 0.28$ $K_s/I = 0.52 + 0.34 \log P + 0.32(\log P)^2$, $\Delta > 0.25$	32
A	Passed all selection criteria		564
		First Overtone	
G	Below minimum period or lacks three-band data	$P < 0.7$	30
F	Exceeds maximum light curve rms	$\sigma(J) > 0.09$, $\sigma(H) > 0.13$, $\sigma(K_s) > 0.2$	20
E	Outlier in color–color relation	$J - K_s = 0.085 + 0.915(J - H)$, $\Delta > 0.14$	13
D	Outlier in NIR amplitude ratios	$H/J = 0.62$, $\Delta > 0.26$ $K_s/J = 0.61$, $\Delta > 0.24$ $H/K_s = 1.07$, $\Delta > 0.41$	84
C	Phase difference of maximum light	$\Delta\phi(I, JHK_s) \notin (0.05, 0.35)$	14
B	Outlier in NIR-to-I amplitude ratios	$J/I = 0.64$, $\Delta > 0.13$ $H/I = 0.44$, $\Delta > 0.15$ $K_s/I = 0.42$, $\Delta > 0.14$	25
A	Passed all selection criteria		365

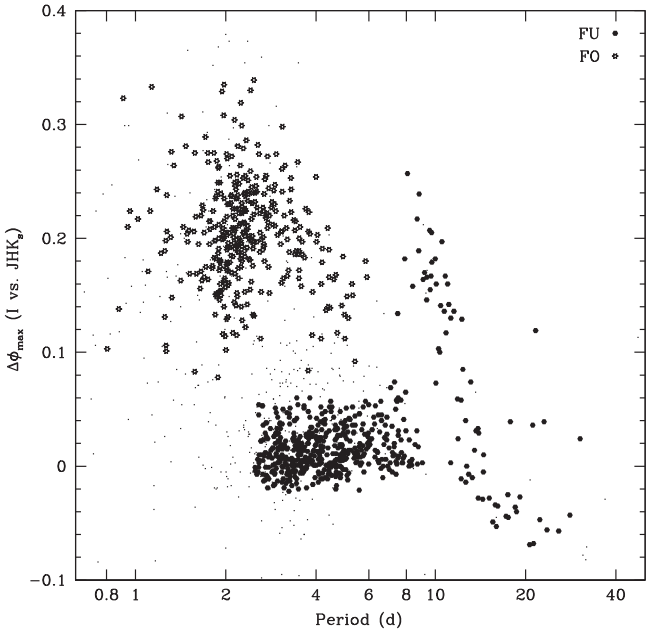

Figure 11. Phase difference for maximum light in JHK_s vs. I for the Cepheids in our sample with the highest-quality light curves (filled and open symbols represent fundamental-mode and first-overtone variables, respectively, while small dots represent variables with lower-quality light curves.

with the total number of stars present in each field, as seen on the right panels of that Figure.

We determined crowding corrections for every star in our catalog by fitting the bias-magnitude relation for its given field and filter over the magnitude range $-1 < m < 0.15$ with a fourth-degree polynomial. We removed from our catalog magnitude measurements that would have required a crowding correction exceeding 0.25 mag, as the uncertainties for larger corrections cannot be reliably determined. The crowding bias is negligible for our field standards and only amounts to a few mmag for the overwhelming majority of the Cepheids (see Section 3.2 for details).

3. RESULTS

3.1. Ensemble Photometry

While the primary goal of this survey was to obtain well-sampled light curves of Cepheid variables, the ensemble photometry obtained as a byproduct can be used to characterize other distance indicators. The coordinates, fully calibrated mean magnitudes and variability indices of stars with photometry in at least two bands are listed in Appendix Table A1. The color–magnitude/Hess diagrams plotted in Figure 6 show that stars in the red giant branch (RGB) constitute the majority of the objects in our photometric catalog. The luminosity functions of all stars in our catalog with $J - H > 0.4$ mag (for J and H) or $J - K_s > 0.5$ (for K_s) are plotted in Figure 7, indicating a clear detection of the tip of the RGB (TRGB) at all wavelengths and the red clump (RC) in J and H.

We determined the TRGB magnitudes by selecting stars over a narrower color range ($0.75 < J - H < 1.0$ for the J and H LFs, and $0.95 < J - K_s < 1.3$ for the K_s LF), calculating Gaussian-smoothed luminosity functions as defined in Equation (A1) of Sakai et al. (1996) (setting a minimum value of $\sigma_i = 0.01$ mag) and applying the modified Sobel edge-detection filter as implemented in Equation (4) of Méndez et al. (2002) (with $\bar{\sigma}_m = 0.025$ mag). The parameter choices were motivated by the very small (few mmag) internal measurement uncertainties for stars near the TRGB. We identified the local maximum of the edge-detection function in the vicinity (± 0.3 mag) of the TRGB and fit it with a spline to determine its peak value. We characterized the uncertainty in our measurements by carrying out 400 bootstrap realizations of this procedure, in which the magnitudes were perturbed by their errors. We obtained TRGB magnitudes of $J = 13.23 \pm 0.03$, $H = 12.35 \pm 0.02$ and $K_s = 12.11 \pm 0.01$ mag.

We determined the RC magnitudes by fitting the LFs of stars with $0.4 < J - H < 1.0$ mag using the following function:

$$\Phi(m) = I(m)\left(10^{\,a+bm} + c\ \exp\left\{-(m - m_{\rm RC})^2 \Big/ \left(2\sigma_{\rm RC}^2\right)\right\}\right), \quad (2)$$

where a and c are normalization factors, b is the slope of the RGB LF, $m_{\rm RC}$ and $\sigma_{\rm RC}$ are the mean magnitude and Gaussian width of the RC, respectively. $I(m)$ models the photometric incompleteness as a function of magnitude,

$$I(m) = 1 \Big/ \left(1 + \exp\left\{(m - m_I)/\xi_I\right\}\right), \quad (3)$$

where m_I is the magnitude at which the incompleteness reaches 50% and ξ_I gives the scale length of the incompleteness cutoff. Figure 8 shows a typical fit to the luminosity functions for one of our fields, and Table 1 summarizes the mean values of the various parameters. We found $\langle m_{\rm RC} \rangle = 17.60 \pm 0.03$ and 16.95 ± 0.04 mag in J and H, respectively. We were unable to determine a reliable measurement of $m_{\rm RC}$ at K_s due to the severe incompleteness of our photometry and the significantly larger crowding corrections at the expected RC magnitude ($K_s \sim 16.9$ mag).

3.2. Cepheid Sample and Light Curves

Our Cepheid sample is based on the catalogs produced by the OGLE-III project (Soszyński et al. 2008; Ulaczyk et al. 2013), which provide very high-quality uniform optical photometry, mode classification and light curve parameters such as period and time of maximum light in I (hereafter $T_{I,\rm max}$). We identified 866 fundamental-mode (hereafter, FU) and 551 first-overtone (hereafter, FO) variables within our survey area, covering the period range of $1.14 < P < 52.9$ days for FU and $0.27 < P < 5.91$ days for FO. The fully calibrated light curve data for all Cepheids (including photometric zeropoints, color terms and crowding corrections) is provided in Table 2. The crowding corrections for the FU variables were no larger than 7 mmag in J and H, and only greater than 10 mmag for 3% of the objects in K_s. The corrections were slightly more significant for the fainter FO variables, exceeding 10 mmag for 4%, 0.5% and 9% of the variables in J, H and K_s, respectively.

We phased the Cepheid magnitudes using the periods and $T_{I,\rm max}$ from the aforementioned OGLE-III catalogs and fit the light curves using the templates of Soszyński et al. (2005) for FU variables and sinusoidal templates for the FO variables. Figures 9 and 10 show representative light curves and their corresponding template fits for FU and FO variables, respectively. We independently solved for the light curve amplitude in each band and we solved for a common phase offset between maximum light in JHK_s and I (hereafter, $\Delta\phi(I, JHK_s)$). We calculated mean magnitudes through

Table 5
Additional Cepheids from Persson et al. (2004)

ID	P (days)	Mean Magnitudes					σ			E_{VI}	UF	Src
		V	I	J	H	K_s	J	H	K_s			
HV5541	2.682	15.970	15.350	14.928	14.658	14.593	50	35	61	42	Y	S02
HV12225	3.007	16.160	15.420	14.950	14.629	14.537	16	16	27	42	Y	S02
HV12765	3.429	15.290	14.670	14.174	13.904	13.840	14	12	12	73	Y	S02
HV12747	3.599	15.770	15.130	14.641	14.347	14.279	22	18	16	42	Y	S02
HV12226	3.706	15.874	15.161	14.517	14.169	14.182	50	51	183	51	Y	S14
OGL-3320	4.785	15.304	14.628	14.121	13.820	13.744	21	16	16	20	Y	S08
OGL-3258	6.838	15.188	14.405	13.827	13.486	13.397	13	10	10	110	Y	S08
HV13048	6.853	...	...	13.675	13.349	13.265	23	16	13	51	Y	N/A
OGL-1128	6.863	15.050	14.291	13.756	13.435	13.337	21	16	16	80	Y	S08
OGL-1327	6.924	15.151	14.355	13.831	13.486	13.403	16	13	13	80	Y	S08
HV12700	8.153	14.860	14.110	13.480	13.141	13.047	10	9	10	80	Y	S02
HV2854	8.635	14.650	13.870	13.314	12.969	12.883	13	10	10	14	Y	S02
HV2733	8.722	14.680	13.960	13.389	13.043	12.963	11	9	8	80	Y	S02
OGL-0107	8.739	14.755	13.941	13.349	13.015	12.925	18	15	14	150	Y	S08
OGL-0046	8.844	14.733	13.950	13.368	13.041	12.944	23	17	17	110	Y	S08
HV12816	9.108	14.490	13.850	13.335	13.049	12.969	15	10	9	51	Y	S02
HV971	9.297	14.480	13.730	13.194	12.847	12.763	19	14	14	42	Y	S02
OGL-1538	10.918	14.227	13.507	12.970	12.643	12.554	17	14	13	100	Y	S08
OGL-1954	12.950	14.615	13.670	13.069	12.675	12.556	22	21	20	90	Y	S08
OGL-0655	12.988	14.898	13.939	13.248	12.851	12.722	24	26	23	70	Y	S08
OGL-2337	13.143	14.591	13.635	12.957	12.566	12.440	21	18	16	180	Y	S08
OGL-3203	13.400	14.153	13.333	12.793	12.443	12.359	14	10	9	90	Y	S08
HV2579	13.431	14.040	13.240	12.672	12.324	12.222	23	16	14	73	Y	S02
OGL-1100	13.633	14.185	13.359	12.786	12.440	12.338	19	15	14	70	Y	U13
HV955	13.732	14.020	13.240	12.670	12.332	12.237	26	19	18	42	Y	S02
OGL-0070	13.746	14.761	13.750	13.067	12.646	12.533	19	20	22	150	Y	S08
OGL-2030	13.871	14.475	13.468	12.849	12.443	12.329	14	14	16	80	Y	S08
OGL-0500	13.978	14.255	13.490	12.786	12.413	12.312	20	18	17	90	Y	S08
OGL-1184	14.212	14.563	13.578	12.956	12.544	12.429	23	22	24	90	Y	S08
OGL-2636	14.216	14.398	13.478	12.753	12.366	12.254	26	23	23	180	Y	S08
OGL-0683	14.677	14.332	13.427	12.773	12.382	12.285	22	21	23	60	Y	S08
OGL-0545	15.831	14.243	13.281	12.627	12.226	12.111	23	22	21	80	Y	S08
OGL-0174	15.863	14.756	13.656	12.889	12.444	12.294	21	20	19	130	Y	S08
OGL-2023	16.223	13.796	12.890	12.406	12.068	11.968	22	20	19	60	Y	S08
HV2580	16.923	14.010	13.140	12.474	12.093	11.985	21	24	21	66	Y	S02
HV2836	17.528	14.630	13.550	12.734	12.267	12.113	21	23	21	132	Y	S02
OGL-2534	18.716	14.123	13.222	12.525	12.132	12.019	30	30	29	140	Y	S08
OGL-2949	19.222	14.089	13.047	12.385	11.945	11.816	24	23	22	170	Y	S08
OGL-0249	20.083	13.946	13.048	12.368	11.963	11.846	35	32	29	80	Y	U13
OGL-0079	22.543	14.116	13.114	12.336	11.907	11.776	33	30	30	140	Y	S08
OGL-0467	22.718	13.666	12.711	12.129	11.756	11.651	32	31	30	60	Y	S08
OGL-2780	23.111	14.580	13.335	12.473	11.947	11.776	17	18	19	200	Y	S08
OGL-0501	23.307	13.522	12.863	12.081	11.725	11.620	30	28	28	90	Y	S08
HV886	23.973	13.470	12.630	11.884	11.527	11.427	30	29	28	42	Y	T99
OGL-2832	24.130	13.830	12.870	12.049	11.616	11.496	23	24	25	80	Y	S08
HV6098	24.238	12.950	12.270	11.717	11.395	11.303	17	16	14	73	Y	S02
OGL-2504	24.336	13.240	12.388	11.814	11.469	11.372	29	24	23	80	Y	U13
HV12815	26.063	13.480	12.540	11.835	11.415	11.297	48	43	35	51	Y	S02
OGL-0999	26.345	13.272	12.371	11.817	11.459	11.364	31	30	27	70	Y	U13
OGL-3158	26.560	13.783	12.750	12.027	11.609	11.484	29	28	27	130	Y	S02,S08
OGL-0654	27.897	13.590	12.530	11.674	11.309	11.206	35	30	29	30	Y	S08
OGL-0068	28.382	13.706	12.633	11.939	11.549	11.421	31	26	25	150	Y	U13
OGL-0367	29.867	13.890	12.734	11.962	11.531	11.408	25	24	23	60	Y	U13
OGL-0434	30.343	12.980	12.164	11.604	11.275	11.178	15	12	11	70	Y	U13
HV1002	30.472	12.950	12.160	11.523	11.176	11.076	32	28	26	73	Y	F85
OGL-0328	34.460	13.027	12.114	11.475	11.100	10.984	30	27	24	90	Y	U13
OGL-0528	35.712	13.064	12.166	11.512	11.133	11.018	34	30	28	50	Y	U13
OGL-0945	36.580	12.738	11.830	11.222	10.858	10.756	38	32	32	30	Y	S08
OGL-1113	37.559	12.760	11.917	11.323	10.974	10.870	30	25	26	80	Y	U13
OGL-0512	39.398	13.031	12.046	11.340	10.935	10.819	35	31	29	90	Y	U13
HV2338	42.239	12.829	11.858	11.170	10.789	10.676	33	29	27	70	Y	B9+
OGL-0461	45.208	13.363	12.232	11.424	10.953	10.821	17	18	17	90	Y	U13
HV953	47.890	12.280	11.390	10.773	10.414	10.303	25	22	22	51	Y	F85

Table 5
(Continued)

ID	P (days)	Mean Magnitudes					σ			E_{VI}	UF	Src
		V	I	J	H	K_s	J	H	K_s			
OGL-1290	48.378	12.590	11.648	10.927	10.525	10.399	28	25	24	80	Y	U13
HV2827	78.860	12.300	11.220	10.414	9.967	9.837	17	17	16	58	Y	M79
HV5497	99.200	11.930	10.880	10.013	9.593	9.452	14	15	15	69	Y	S02

Notes. IDs, periods, and *VI* magnitudes are from the OGLE catalogs (Soszyński et al. 2008; Ulaczyk et al. 2013; I. Soszyński 2014, private communication abbreviated as S08, U13, and S14, respectively) when available or otherwise from the literature (Martin et al. 1979; Freedman et al. 1985; Barnes et al. 1999; Tanvir & Boyle 1999; Sebo et al. 2002; Ngeow & Kanbur 2006) abbreviated as M79, F85, B99, T99, S02, and N06, respectively). Tabulated magnitudes are not corrected for extinction. JHK_s magnitudes have been transformed into the 2MASS system. E_{VI} values are taken from Haschke et al. (2011), when available. Magnitude uncertainties and reddenings are expressed in mmag. UF: flag to indicate if the variable was used in the final P–L fits.

(This table is available in its entirety in machine-readable and Virtual Observatory (VO) forms.)

numerical integration of the best-fit templates and estimated the magnitude uncertainties from the rms of the light curve data about the template. Table 3 lists the Cepheid properties, along with individual reddening values (obtained from the extinction map of Haschke et al. 2011), a quality flag, and a flag to identify variables that were used in our final Leavitt Law fits (see Section 3.3 for details).

We classified our light curves into several quality bins, listed in Table 4 to later investigate any possible influence in our fits. Figure 11 highlights the variation in $\Delta\phi(I, JHK_s)$ versus log P for the highest-quality variables in the FU and FO samples. We observe a mild dependence of this parameter with period for FU variables with $P < 8$ days, and the gap due the Hertzsrpung progression is nicely detected. This topic is further explored in Bhardwajj et al. (2014).

As an external check of our procedures for photometric calibration and determination of mean magnitudes, we compared the values obtained for 23 Cepheids in common with P04. We transformed their magnitudes using the relations between the LCO and the 2MASS systems given in section VI.4.b of Cutri et al. (2003a):

$$K_{s,2} - K_{s,\mathrm{L}} = 0.002\left(J - K_s\right)_{\mathrm{L}} - 0.015,$$
$$\left(J - K_s\right)_2 = 1.012\left(J - K_s\right)_{\mathrm{L}} - 0.007,$$
$$\left(H - K_s\right)_2 = 1.015\left(H - K_s\right)_{\mathrm{L}} + 0.003,$$

where the "2" and "L" subscripts refer to 2MASS and LCO magnitudes, respectively. We found offsets (P04–this work) of -10 ± 9, 8 ± 8, and 3 ± 6 mmag in JHK_s, respectively.

3.3. Leavitt Laws

We corrected the mean magnitudes listed in Table 3 for the effects of interstellar dust using individual reddening values derived from the map of Haschke et al. (2011) and the extinction law of Fitzpatrick (1999) applicable to the LMC. We adopted $R_V = 3.1$, which for this extinction law yields ratios of total-to-selective absorption of $A_J = 1.0881$, $A_H = 0.6917$ and $A_K s = 0.4505$ per mag of E_{VI}.

We increased the period range of the sample by adding 66 fundamental-mode variables with $P < 100$ days from P04 that were not already in common with our catalog. Their magnitudes were transformed into the 2MASS system using the aforementioned relations and corrected for extinction using the same procedure as above. For those variables lying outside of the extinction map of Haschke et al. (2011), we used the $E(B-V)$ values tabulated in P04. For completeness, the properties of these variables are listed in Table 5.

We solved for Leavitt Laws and period–luminosity–color relations of the form

$$m = a + b(\log P - 1) \quad (4)$$

$$m = a + b(\log P - 1) + c\left(J - K_s\right) \quad (5)$$

following two basic assumptions: (i) the relations obey a single slope b over the period range being considered; (ii) the residuals of any given Cepheid about the best-fit Leavitt Law should exhibit a strong correlation arising as a consequence of (a) uncorrected extinction or line of sight depth effects and/or (b) the intrinsic width in temperature of the instability strip and the resulting variation in luminosity as a function of temperature for a fixed period (for a comprehensive review, see Madore & Freedman 1991).

We started the fits using all variables except those with quality flag G, which are objects without three-band photometry or lying below the minimum period limits (hereafter, P_{min}) of 0.7 and 2.5 days for FO and FU, respectively. We carried out the fits in an iterative manner, removing the single largest $>3\sigma$ outlier in each of the three residual relations (ΔJ versus ΔH, ΔJ versus ΔK_s, ΔH versus ΔK_s) until convergence. Figures 12 and 13 show the final Leavitt Laws for FU and FO variables, respectively, while Figure 14 shows the correlations of residuals used to identify and remove outliers. The objects included or excluded in the final fits are identified with "Y" or "N" in column 17 of Table 3. Lastly, Figure 15 shows the combined Leavitt Laws plotting only the Cepheids in the final samples.

The results of the fits are summarized in Table 6. We estimated the statistical uncertainties in all the derived parameters by performing 10^4 realizations of the fitting procedure in which the magnitudes were randomly altered according to their measurement errors. In order to preserve the physical correlations of the residuals, the magnitudes of a given Cepheid in all three bands were shifted using the same randomly drawn scale factor. Figures 16 and 17 show the result of this exercise for the FU and FO samples, respectively. The much stronger correlation between parameters for the FO Leavitt Laws, relative to the FU ones, is expected given the much smaller range in period spanned by the former. There is also a significant, but less strong, correlation between P–L–C parameters for both classes.

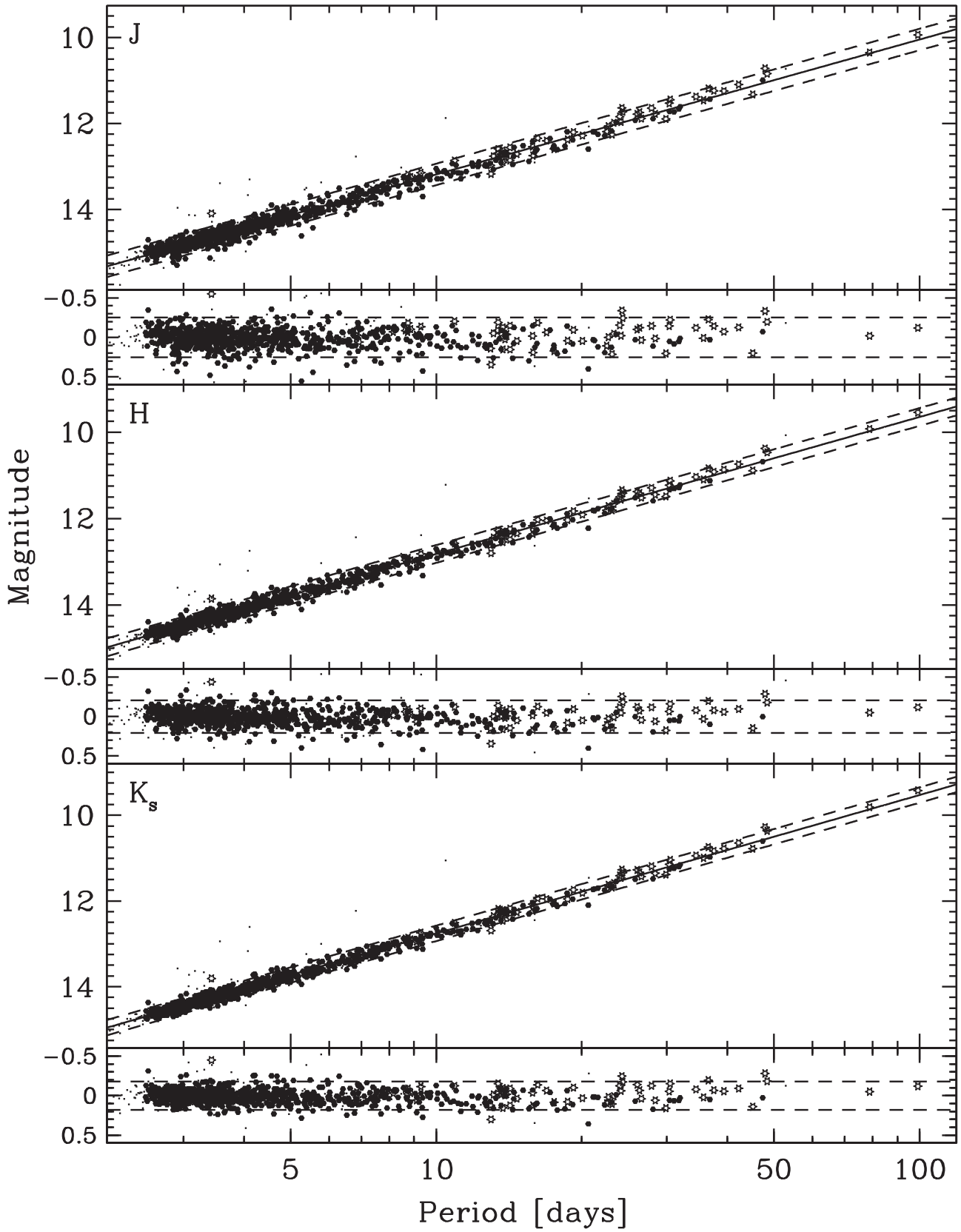

Figure 12. Leavitt Law and residuals in J (top), H (middle), and K_s (bottom) for FU Cepheids, based on 866 objects from our sample (filled symbols) and 66 variables from Persson et al. (2004) (open symbols). Outliers identified through an iterative rejection process based on correlated residuals are plotted using small dots. Dashed lines indicate the $\pm 2\sigma$ widths of the relations.

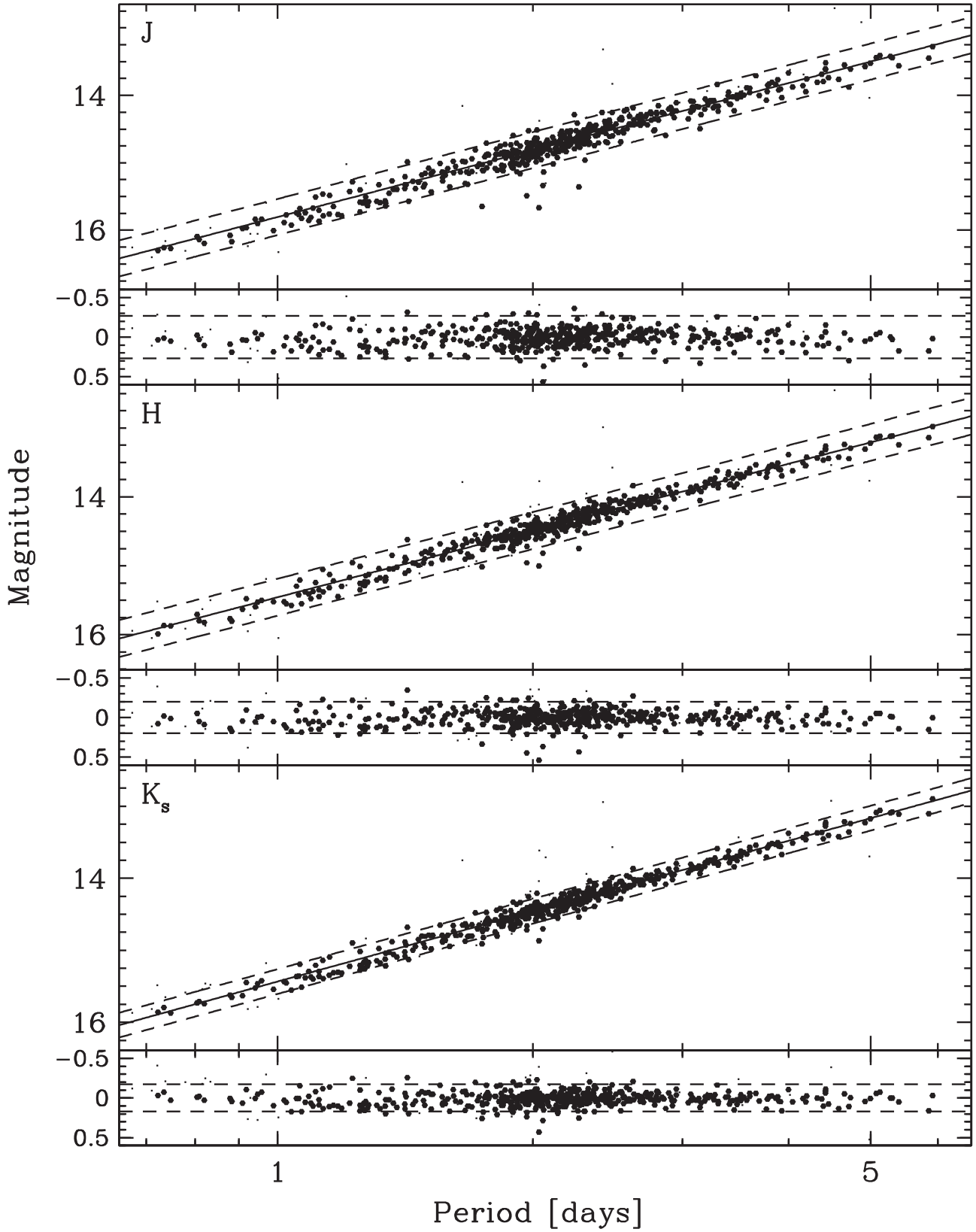

Figure 13. Leavitt Law and residuals in J (top), H (middle), and K_s (bottom) for FO Cepheids, based on 551 objects from our sample (filled symbols). Outliers identified through an iterative rejection process based on correlated residuals are plotted using small dots. Dashed lines indicate the $\pm 2\sigma$ widths of the relations.

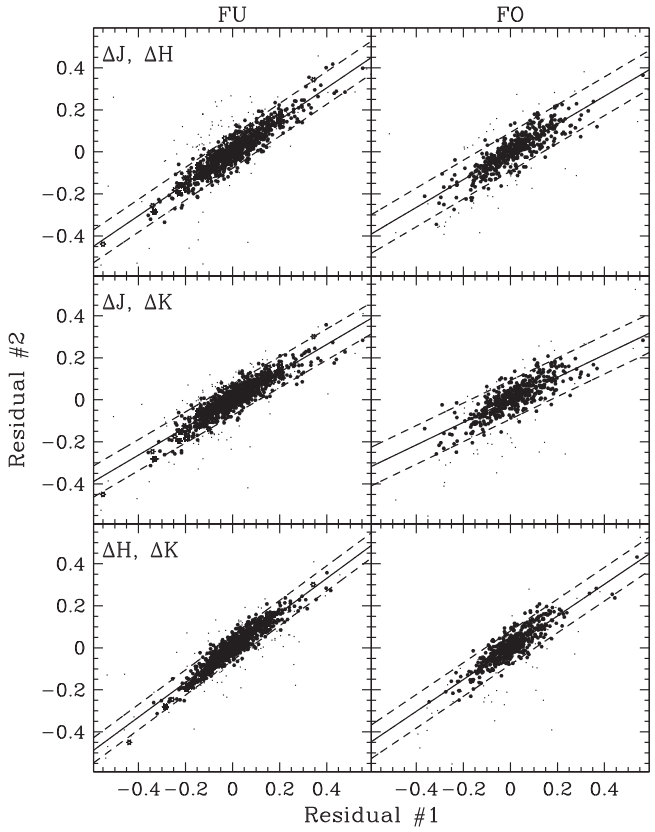

Figure 14. Residuals from the Leavitt Laws plotted in Figures 12 (left) and 13 (right). Plotting symbols follow the same convention as the aforementioned figures.

Our results are in good agreement with those derived by Persson et al. (2004) but provide considerably stronger constraints on the slopes. Transforming the latter into the 2MASS system, we find zeropoint differences (this work–P04) of 0.018 ± 0.067, -0.016 ± 0.058, 0.000 ± 0.054 mag in JHK_s, respectively. The slopes we determined are somewhat shallower but statistically consistent given the larger uncertainties of the previous work, with differences of 0.013 ± 0.053, 0.065 ± 0.042, 0.053 ± 0.040 mag/dex in JHK_s, respectively.

There is also very good agreement with recent theoretical calculations of the average slope over the entire period range of fundamental-mode pulsators (hereafter, $b_{\rm all}$). Following Bono et al. (2010), we calculated "LMC average" values at J and K_s by combining the results for $\log(Z/X) = -2.27$ and -1.97 in their Table 2, and similarly at H based on Table 1 from Fiorentino et al. (2013). We found $b_{\rm all} = -3.15$, -3.19, -3.24 ± 0.05 mag/dex in JHK_s, respectively, which differ by less than 0.02 from the values listed in Table 6.

We explored the sensitivity of the derived Leavitt Law parameters to the subsample of FU Cepheids being considered, by imposing cuts based on light curve quality (Table 4) and $P_{\rm min}$. While we found no statistically significant variation with light curve quality, there is a clear trend in the parameters with respect to the minimum period as shown in Figure 18. The theoretical expectation (Bono et al. 2010; Fiorentino et al. 2013) is for the slopes to become shallower for $P_{\rm min} > 10$ days, as recently detected in the metal-rich Cepheids of M31 (Kodric et al. 2014). However we see the opposite behavior for the LMC Cepheids, with a significant increase in the slope for $P_{\rm min} \geqslant 8$ days. We plan further work in a companion paper to investigate this issue. The large and somewhat noisy variation in the derived values for larger $P_{\rm min}$ emphasizes the importance of obtaining large Cepheid samples to obtain robust parameters for the Leavitt Law.

3.4. Absolute Calibration of the Distance Indicators

We derived absolute calibrations for the TRGB, RC, and the Leavitt Law using the distance to the LMC determined by Pietrzyński et al. (2013) using eight long-period, late-type eclipsing binary systems: $D = 49.97 \pm 2\%$ kpc (equivalent to $\mu_0 = 18.493 \pm 0.048$ mag). We prefer this distance estimate over other contemporaneous results with slightly smaller uncertainties (such as Laney et al. 2012, $18.475 \pm$

Table 6
Leavitt Laws and Period–Luminosity–Color Relations

Band(s)	Zeropoint	Slope	Color Term	rms
Fundamental Mode: $P_{\rm min} = 2.5$ days, $N_{\rm start} = 872$, $N_{\rm final} = 789$				
J	13.185 ± 0.001	-3.140 ± 0.004	...	0.125
H	12.819 ± 0.002	-3.169 ± 0.004	...	0.103
K_s	12.756 ± 0.001	-3.228 ± 0.004	...	0.090
J, $(J-K_s)$	12.364 ± 0.018	-3.307 ± 0.007	1.933 ± 0.042	0.083
H, $(J-K_s)$	12.332 ± 0.018	-3.257 ± 0.007	1.167 ± 0.042	0.086
K_s, $(J-K_s)$	12.364 ± 0.018	-3.307 ± 0.007	0.932 ± 0.042	0.083
First Overtone: $P_{\rm min} = 0.7$ day, $N_{\rm start} = 521$, $N_{\rm final} = 475$				
J	12.507 ± 0.013	-3.297 ± 0.020	...	0.134
H	12.241 ± 0.012	-3.215 ± 0.020	...	0.100
K_s	12.189 ± 0.014	-3.245 ± 0.023	...	0.086
J, $(J-K_s)$	12.071 ± 0.028	-3.265 ± 0.024	1.320 ± 0.065	0.080
H, $(J-K_s)$	12.013 ± 0.032	-3.197 ± 0.024	0.678 ± 0.073	0.083
K_s, $(J-K_s)$	12.071 ± 0.028	-3.265 ± 0.024	0.320 ± 0.065	0.080

Note. Quoted uncertainties in zeropoints and color terms do not include external photometric uncertainties of 11, 18, and 14 mmag in JHK_s, respectively (Section 2.3), which should be added in quadrature to the above values.

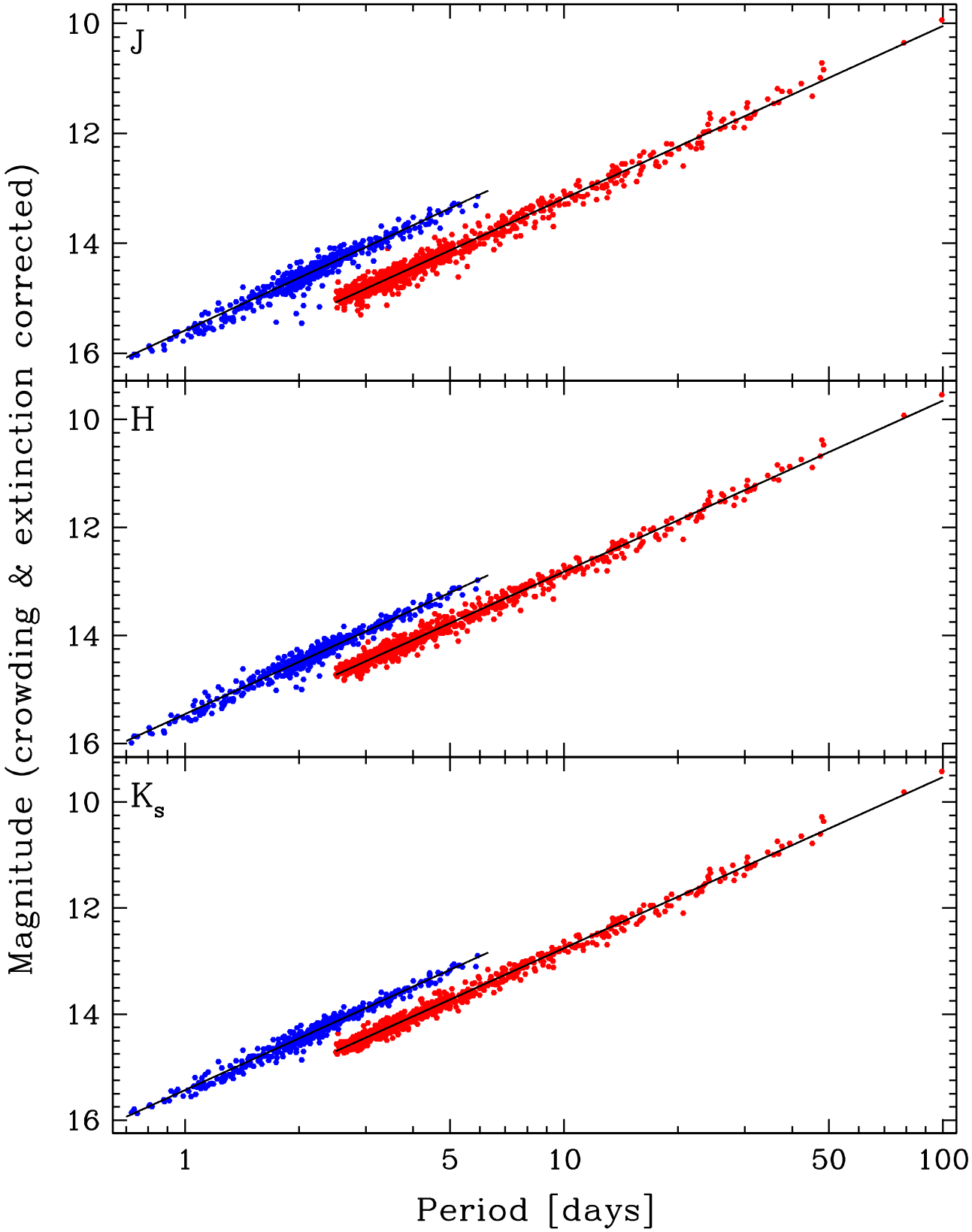

Figure 15. Final Leavitt Laws for FU and FO Cepheids, plotted using filled red and blue symbols, respectively.

0.021 mag) because the method does not depend on stellar population corrections.

We corrected the TRGB magnitudes determined in Section 3.1 for extinction using the same extinction law and total-to-selective extinction values listed above, and adopted the median reddening value in our fields from Haschke et al. (2011), $\langle E_{VI} \rangle = 0.08$ mag. Using the aforementioned distance modulus, we obtained $M_{\rm TRGB} = -5.35 \pm 0.06, -6.20$

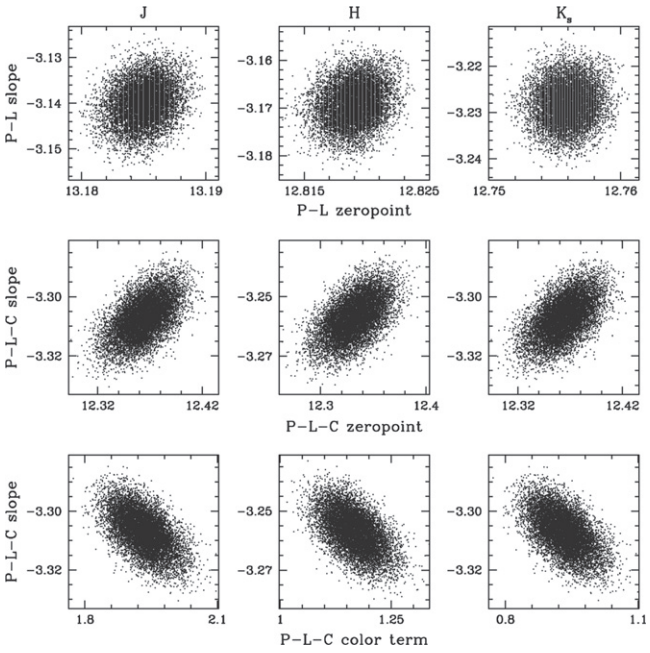

Figure 16. Result of 10^4 random realizations of the P–L and P–L–C fitting procedures for FU Cepheids, used to estimate the statistical uncertainty and correlation of the derived parameters. The limits of each panel span $\pm 4\sigma$ in the respective parameter.

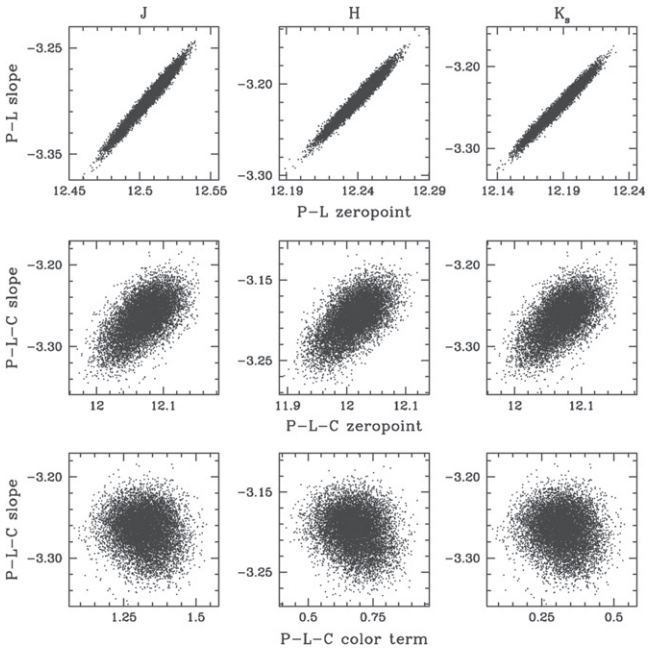

Figure 17. Result of 10^4 random realizations of the P–L and P–L–C fitting procedures for FO Cepheids, used to estimate the statistical uncertainty and correlation of the derived parameters. The limits of each panel span $\pm 4\sigma$ in the respective parameter.

$\pm$ 0.05, -6.41 ± 0.05 mag in JHK_s, respectively. These values are in excellent agreement with recent empirical calibrations (see figure 5 of Bellazzini 2008) which give $M_{\rm TRGB} = -5.44$, -6.30, -6.50 ± 0.10 mag for a population with the same value of $\langle J - K_s \rangle_{0,\rm TRGB}$.

Following the same procedure for the RC measurements, we find $M_{\rm RC} = -0.98 \pm 0.06$ and -1.60 ± 0.07 mag in J and H, respectively. These values can be compared with the local calibration of Laney et al. (2012) based on *Hipparcos* parallaxes, of -0.984 ± 0.014 and -1.490 ± 0.015 mag. Alternatively, using the crowding- and extinction-corrected RC magnitudes and the Laney et al. (2012) absolute calibration we obtain an error-weighted mean LMC distance modulus of 18.46 ± 0.08 mag, which is consistent with the more precise determination by Pietrzyński et al. (2013).

Lastly, using the values listed in Table 6 we find the following absolute calibration of the NIR Leavitt Laws in the LMC for fundamental-mode pulsators:

$$J\text{: } -5.308 \pm 0.051 - 3.140 \pm 0.004\ (\log P - 1) \quad (6)$$

$$H\text{: } -5.674 \pm 0.053 - 3.169 \pm 0.004\ (\log P - 1) \quad (7)$$

$$K_s\text{: } -5.736 \pm 0.051 - 3.228 \pm 0.004\ (\log P - 1), \quad (8)$$

which includes fully propagated uncertainties in the zeropoint due to intrinsic dispersion, photometric calibration and distance modulus.

4. SUMMARY

We have presented the details of a near-infrared (JHK_s) synoptic survey of the central region of the LMC, with the primary goal of providing the largest sample to date of multi-wavelength, time-resolved observations of Cepheid variables in this region of the electromagnetic spectrum. Our sample is derived from optical observations by the OGLE project (Soszyński et al. 2008) and also benefits from an extension to longer periods by Persson et al. (2004). The combined sample increases by a factor of 9 the number of available light curves with this type of data for fundamental-mode pulsators, yielding a significant increase in the accuracy with which the Leavitt Law slopes are determined. We find slopes in excellent agreement with theoretical predictions for the full period range, but we observe an unexpected steepening at long periods. We have taken advantage of the precise and accurate determination of the LMC distance using eclipsing binaries (Pietrzyński et al. 2013) to update the absolute calibration of the Leavitt Law at these wavelengths. Furthermore, we have used our photometric database to obtain a robust absolute calibration of the TRGB and to detect the RC.

We plan further work based on our catalog to carry out a Fourier analysis of Cepheid light curve structure (Bhardwaj et al. 2015), a study of nonlinearity in the Leavitt Law and P–L relations of long-period variables, among other topics.

L.M.M. acknowledges support by: NASA through Hubble Fellowship grant *HST*-HF-01153 from the Space Telescope Science Institute; NSF through a Goldberg Fellowship from the National Optical Astronomy Observatory and AST grant #1211603; Texas A&M University through a faculty start-up fund and the Mitchell-Heep-Munnerlyn Endowed Career Enhancement Professorship in Physics or Astronomy. S.M.K. thanks SUNY-Oswego for startup funds that funded much of the initial telescope time. This research was supported by the Munich Institute for Astro- and Particle Physics (MIAPP) of the DFG cluster of excellence "Origin and Structure of the universe." L.M.M. and S.M.K. also thank the Indo-US Science and Technology Forum for supporting collaborative visits during which some of this work was completed. C.C.N. acknowledges funding from the Ministry of Science and Technology of Taiwan under contract NSC101-2112-M-008-

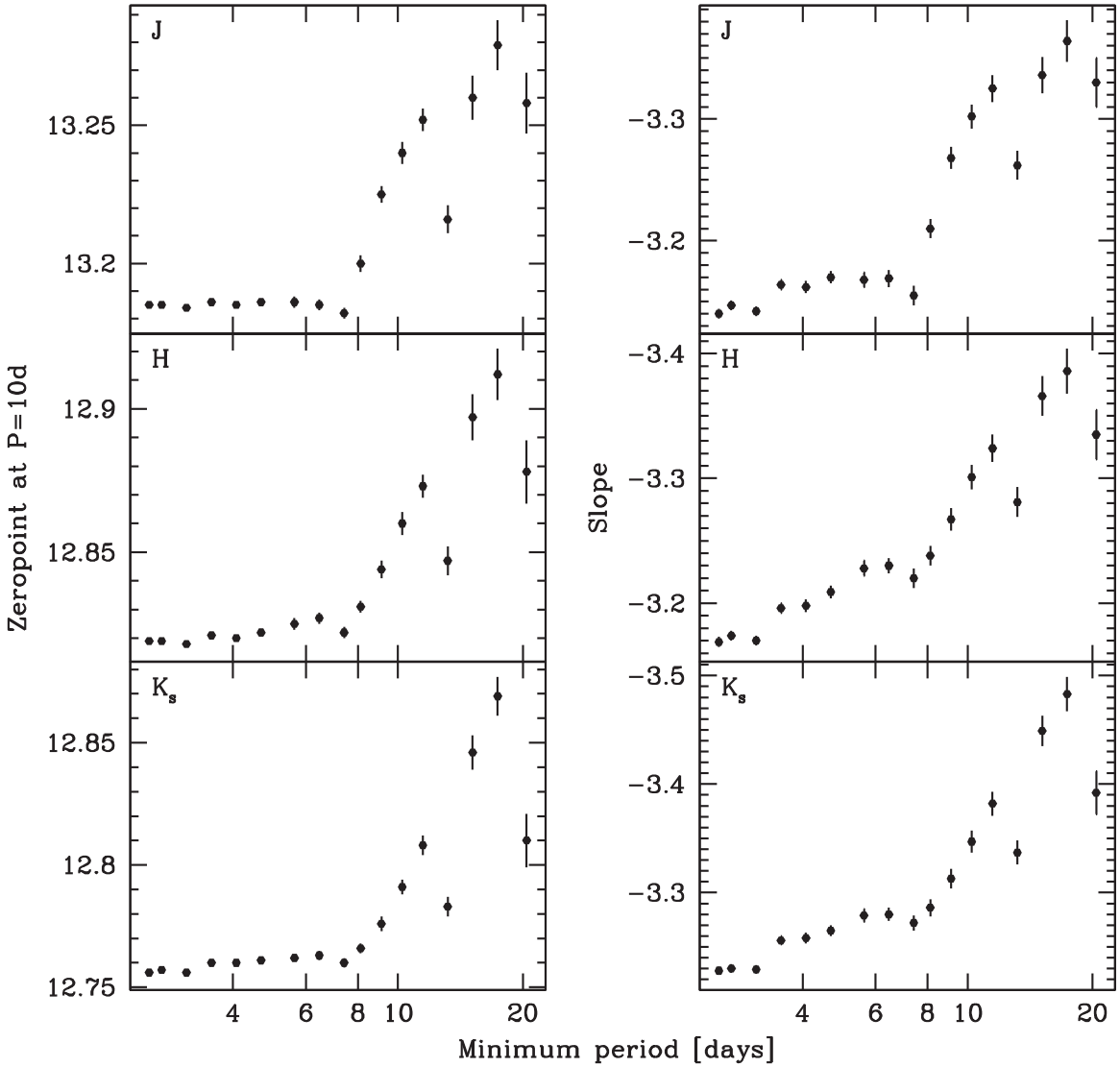

Figure 18. Changes in Leavitt Law parameters for FU Cepheids when restricting the sample by minimum period.

017-MY3. We thank Frank Ripple for assistance with the initial data reduction, and the anonymous referee for helpful comments.

This publication has made use of the following resources.

1. Observations obtained at the 1.5 m telescope of the Cerro Tololo Inter-American Observatory, operated by the SMARTS Consortium. CTIO is part of the National Optical Astronomy Observatory, which is operated by the Association of Universities for Research in Astronomy under contract with the National Science Foundation.
2. Data products from the Optical Gravitational Lensing Experiment, conducted by the Astronomical Institute of the University of Warsaw at Las Campanas Observatory, operated by the Carnegie Institution for Science.
3. Data products from 2MASS, which is a joint project of the University of Massachusetts and the Infrared Processing and Analysis Center at the California Institute of Technology, funded by the National Aeronautics and Space Administration and the National Science Foundation.
4. The Digitized Sky Surveys, produced at the Space Telescope Science Institute under U.S. Government grant NAG W-2166. The images of these surveys are based on photographic data obtained using the Oschin Schmidt Telescope on Palomar Mountain and the UK Schmidt Telescope.
5. NASA's Astrophysics Data System at the Harvard–Smithsonian Center for Astrophysics.
6. The SIMBAD database and the VizieR catalog access tool, operated at CDS, Strasbourg, France.
7. The McMaster Cepheid Photometry and Radial Velocity Data Archive, maintained by Prof. D. Welch at McMaster University, Canada.

Facility: CTIO:1.5 m

APPENDIX

Table A1 presents the coordinates, fully calibrated mean magnitudes, and variability indices of all stars detected in our observations with photometry in at least two bands.

Table A1
Ensemble Photometry

Coordinates (J2000.)		Magnitudes			σ (Mag)			J_{Stet}			Field
R.A.	Decl.	J	H	K_s	J	H	K_s	J	H	K_s	#
74.28737	−69.54611	...	13.661	13.404	...	0.005	0.007	...	0.356	0.309	2
74.28782	−69.57628	14.930	14.114	14.028	0.009	0.008	0.013	0.372	0.394	0.384	2
74.28901	−69.53095	15.686	14.859	14.813	0.012	0.012	0.019	0.123	0.627	0.278	2
74.28933	−69.57615	16.532	...	15.511	0.045	...	0.050	0.875	...	0.456	2
74.28983	−69.49224	16.581	16.440	...	0.018	0.028	...	0.305	0.194	...	2
74.29041	−69.57333	14.442	13.720	13.439	0.007	0.009	0.010	0.061	0.645	0.261	2
74.29078	−69.52931	18.086	17.233	...	0.047	0.050	...	0.111	0.046	...	2
74.29169	−69.51814	16.909	15.843	15.742	0.024	0.019	0.038	0.069	0.166	0.021	2
74.29231	−69.48591	17.086	16.348	...	0.025	0.029	...	0.240	0.247	...	2
74.29240	−69.56323	17.482	16.941	...	0.034	0.040	...	0.046	0.135	...	2
74.29272	−69.49051	18.174	17.297	...	0.047	0.049	...	−0.125	0.037	...	2
74.29286	−69.48217	17.871	17.043	...	0.037	0.040	...	0.016	0.031	...	2
74.29290	−69.57480	18.042	17.392	...	0.048	0.051	...	0.122	0.023	...	2
74.29321	−69.43479	...	15.553	15.676	...	0.015	0.028	...	0.401	0.005	2
74.29328	−69.56466	18.203	17.497	...	0.047	0.050	...	0.024	0.032	...	2
74.29328	−69.47811	17.388	16.602	...	0.025	0.031	...	0.017	0.053	...	2
74.29331	−69.37026	12.523	12.393	...	0.005	0.006	...	0.164	0.283	...	2
74.29369	−69.52740	18.156	17.105	...	0.053	0.042	...	0.091	−0.035	...	2

Note. Magnitudes were corrected for crowding using the procedure detailed in Section 2.4, but have not been corrected for extinction. Objects with $J_{Stet} > 0.75$ are likely to be variable; mean magnitudes should be considered approximate.

(This table is available in its entirety in machine-readable and Virtual Observatory (VO) forms.)

REFERENCES

Alcock, C., Allsman, R. A, Alves, D. R., et al. 1999, AJ, 117, 920
Artigau, E., Doyon, R., Vallee, P., Riopel, M., & Nadeau, D. 2004, Proc. SPIE, 5492, 1479
Barnes, T. G., III, Ivans, I. I., Martin, J. R., Froning, C. S., & Moffett, T. J. 1999, PASP, 111, 812
Bellazzini, M. 2008, MmSAI, 79, 440
Bhardwaj, A., Kanbur, S., Singh, H., Macri, L., & Ngeow, C. 2015, MNRAS, 447, 3342
Bono, G., Caputo, F., Marconi, M., & Musella, I. 2010, ApJ, 715, 277
Cioni, M.-R. L., Clementini, G., Girardi, L., et al. 2011, A&A, 527, A116
Cutri, R. M., Skrutskie, M. F., van Dyk, S., et al. 2003a, Explanatory Supplement to the 2MASS All Sky Data Release and Extended Mission Products (Pasadena, CA: NASA/IPAC Infrared Science Archive), http://ipac.caltech.edu/2mass/releases/allsky/doc/
Cutri, R. M., Skrutskie, M. F., van Dyk, S., et al. 2003b, The IRSA 2MASS All-Sky Point Source Catalog (NASA/IPAC Infrared Science Archive)
Fiorentino, G., Musella, I., & Marconi, M. 2013, MNRAS, 434, 2866
Fitzpatrick, E. L. 1999, PASP, 111, 63
Freedman, W. L., Grieve, G. R., & Madore, B. F. 1985, ApJS, 59, 311
Haschke, R., Grebel, E. K., & Duffau, S. 2011, AJ, 141, 158
Hubble, E. P. 1925, ApJ, 62, 409
Kato, D., Nagashima, C., Nagayama, T., et al. 2007, PASJ, 59, 615
Kodric, M., Riffeser, A., Seitz, S., et al. 2015, ApJ, 799, 144
Laney, C. D., Joner, M. D., & Pietrzyński, G. 2012, MNRAS, 419, 1637
Leavitt, H. S., & Pickering, E. C. 1912, HarCi, 173, 1
Madore, B. F., & Freedman, W. L. 1991, PASP, 103, 933
Martin, W. L., Warren, P. R., & Feast, M. W. 1979, MNRAS, 188, 139
Méndez, B., Davis, M., Moustakas, J., et al. 2002, AJ, 124, 213
Mink, D. J. 2002, in ASP Conf. Ser. 281, Astronomical Data Analysis Software and Systems XI , ed. D. A. Bohlender, D. Durand, & T. H. Handley (San Francisco, CA: ASP), 169
Ngeow, C.-C., & Kanbur, S. M. 2005, MNRAS, 360, 1033
Ngeow, C.-C., & Kanbur, S. M. 2006, MNRAS, 369, 723
Nikolaev, S., Drake, A. J., Keller, S. C., et al. 2004, ApJ, 601, 260
Persson, S. E., Madore, B. F., Krzemiński, W., et al. 2004, AJ, 128, 2239
Pietrzyński, G., Graczyk, D., Gieren, W., et al. 2013, Natur, 495, 76
Riess, A. G., Macri, L., Casertano, S., et al. 2011, ApJ, 730, 119
Ripepi, V., Moretti, M. I., Marconi, M., et al. 2012, MNRAS, 424, 1807
Sakai, S., Madore, B. F., & Freedman, W. L. 1996, ApJ, 461, 713
Sebo, K. M., Rawson, D., Mould, J., et al. 2002, ApJS, 142, 71
Skrutskie, M. F., Cutri, R. M., Stiening, R., et al. 2006, AJ, 131, 1163
Soszyński, I., Gieren, W., & Pietrzyński, G. 2005, PASP, 117, 823
Soszyński, I., Poleski, R., Udalski, A., et al. 2008, AcA, 58, 163
Stetson, P. B. 1987, PASP, 99, 191
Stetson, P. B. 1993, in IAU Coll. 136, Stellar Photometry—Current Techniques and Future Developments, ed. C. J. Butler & I. Elliott (Cambridge: Cambridge Univ. Press), 291
Stetson, P. B. 1994, PASP, 106, 250
Stetson, P. B. 1996, PASP, 108, 851
Tanvir, N. R., & Boyle, A. 1999, MNRAS, 304, 957
Udalski, A., Soszyński, I., Szymański, M., et al. 1999, AcA, 49, 223
Ulaczyk, K., Szymański, M. K., Udalski, A., et al. 2013, AcA, 63, 159
Weinberg, D. H., Mortonson, M. J., Eisenstein, D. J., et al. 2013, PhR, 530, 87

The Astronomical Journal, 151:48 (3pp), 2016 February doi:10.3847/0004-6256/151/2/48

ERRATUM: "LARGE MAGELLANIC CLOUD NEAR-INFRARED SYNOPTIC SURVEY. I. CEPHEID VARIABLES AND THE CALIBRATION OF THE LEAVITT LAW" (2015, AJ, 149, 117)

Lucas M. Macri[1], Chow-Choong Ngeow[2], Shashi M. Kanbur[3], Salma Mahzooni[1], and Michael T. Smitka[1]
[1] Mitchell Institute for Fundamental Physics & Astronomy, Department of Physics & Astronomy, Texas A&M University, College Station, TX 77843, USA
[2] Graduate Institute of Astronomy, National Central University, Jhongli 32001, Taiwan
[3] Department of Physics, The State University of New York at Oswego, Oswego, NY 13126, USA
Received 2015 December 17; published 2016 February 4

The values of total-to-selective absorption listed in Section 3.3 were incorrectly calculated due to a programming error. We thank Adam Riess for pointing this out. The correct values should have been $A_J = 0.5856$, $A_H = 0.3723$, $A_{Ks} = 0.2425$ per mag of $E(V - I)$. This resulted in small over-corrections for extinction of 0.040, 0.025, 0.017 mag in JHK_s, respectively.

Revised values of the results originally listed in Section 3.4 that are affected by this change are as follows: $M_{\rm TRGB} = -5.31 \pm 0.06$, -6.17 ± 0.05, -6.40 ± 0.05 mag in JHK_s, respectively; $M_{\rm RC} = -0.94 \pm 0.06$ and -1.57 ± 0.07 mag in J and H, respectively; error-weighted mean LMC distance modulus based on red clump stars of 18.49 ± 0.09 mag. The absolute calibrations of the Leavitt Law at JHK_s become

$$J : -5.265 \pm 0.051 - 3.156 \pm 0.004\ (\log P - 1) \quad (6)$$

$$H : -5.646 \pm 0.053 - 3.187 \pm 0.004\ (\log P - 1) \quad (7)$$

$$K_s : -5.717 \pm 0.051 - 3.247 \pm 0.004\ (\log P - 1). \quad (8)$$

The following Cepheids listed in Table 3 are no longer used in the final P-L fits and their entries in Column 17 ("UF") now read "N": 0482, 1009, 1120, 1849, 1938, 2286, 2564, 2629, 2687, 2745, 2764, 2796, 2811, 2841. Similarly, HV 12765 from Table 5 is no longer used in the final P-L fits.

Updated versions of Table 6 and Figures 12–18 are included below.

Table 6
Leavitt Laws and Period–Luminosity–Color Relations

Band(s)	Zeropoint	Slope	Color term	rms
Fundamental mode: $P_{\rm min} = 2.5$ d, $N_{\rm start} = 872$, $N_{\rm final} = 775$				
J	13.228 ± 0.002	-3.156 ± 0.004	...	0.120
H	12.847 ± 0.001	-3.187 ± 0.004	...	0.101
K_s	12.776 ± 0.001	-3.247 ± 0.004	...	0.087
J, $(J - K_s)$	12.397 ± 0.015	-3.311 ± 0.005	1.847 ± 0.033	0.080
H, $(J - K_s)$	12.365 ± 0.014	-3.260 ± 0.005	1.086 ± 0.032	0.084
K_s, $(J - K_s)$	12.397 ± 0.015	-3.311 ± 0.005	0.848 ± 0.033	0.080
First overtone: $P_{\rm min} = 0.7$ d, $N_{\rm start} = 521$, $N_{\rm final} = 474$				
J	12.541 ± 0.012	-3.319 ± 0.020	...	0.131
H	12.262 ± 0.012	-3.227 ± 0.020	...	0.100
K_s	12.201 ± 0.014	-3.257 ± 0.023	...	0.085
J, $(J - K_s)$	12.079 ± 0.030	-3.270 ± 0.024	1.318 ± 0.065	0.080
H, $(J - K_s)$	12.013 ± 0.032	-3.200 ± 0.024	0.698 ± 0.070	0.083
K_s, $(J - K_s)$	12.079 ± 0.030	-3.270 ± 0.024	0.316 ± 0.065	0.080

Note. Quoted uncertainties in zeropoints and color terms do not include external photometric uncertainties of 11, 18, and 14 mmag in JHK_s, respectively (Section 2.3), which should be added in quadrature to the above values.

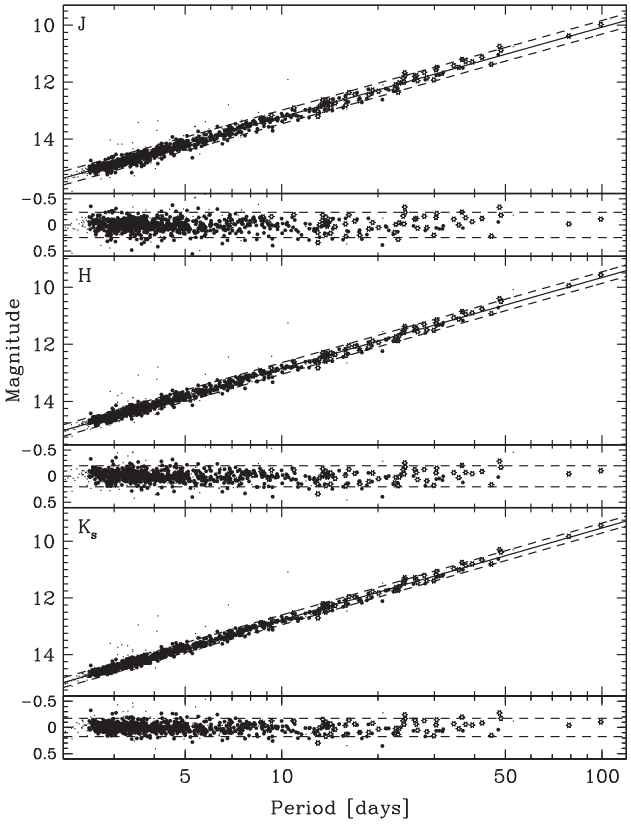

Figure 12. Leavitt Law and residuals in J (top), H (middle) and K_s (bottom) for FU Cepheids.

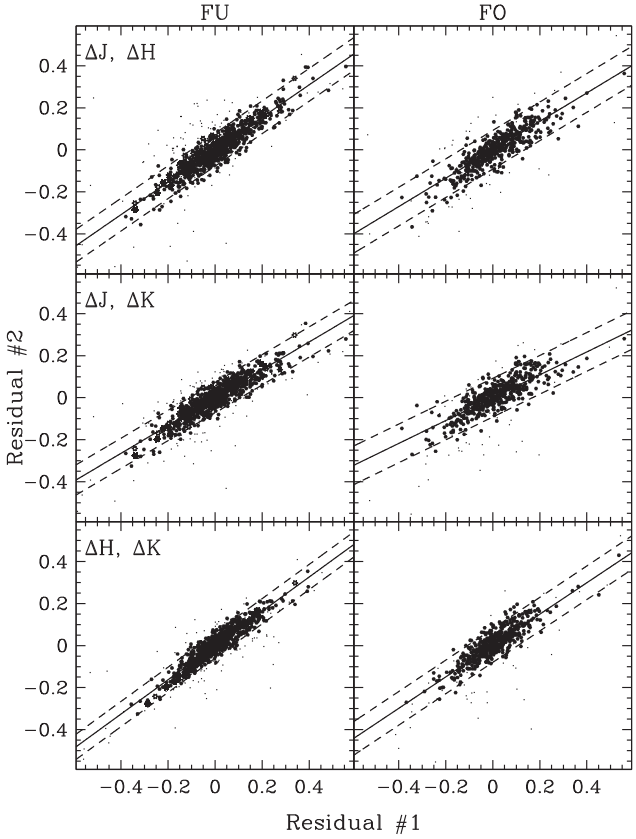

Figure 14. Residuals from the Leavitt Laws plotted in Figures 12 (left) and 13 (right).

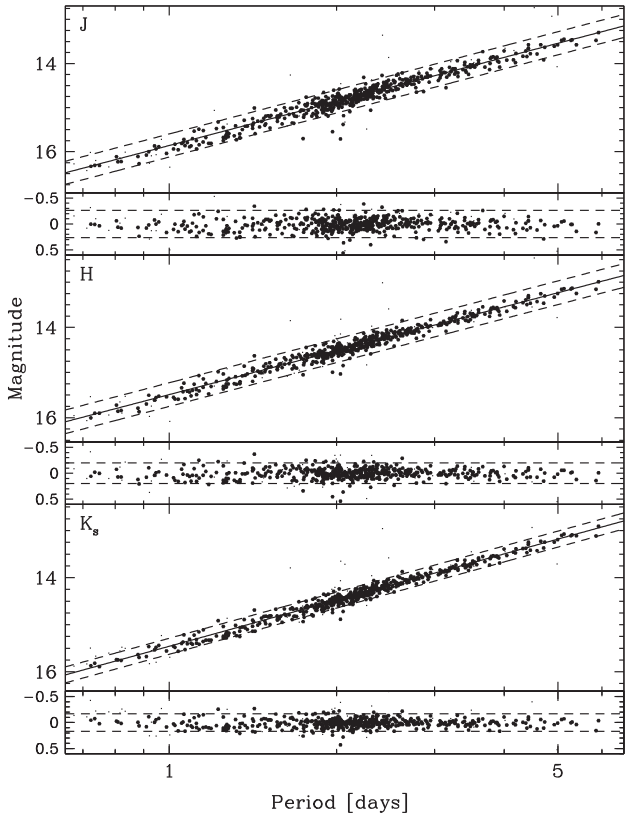

Figure 13. Leavitt Law and residuals in J (top), H (middle) and K_s (bottom) for FO Cepheids.

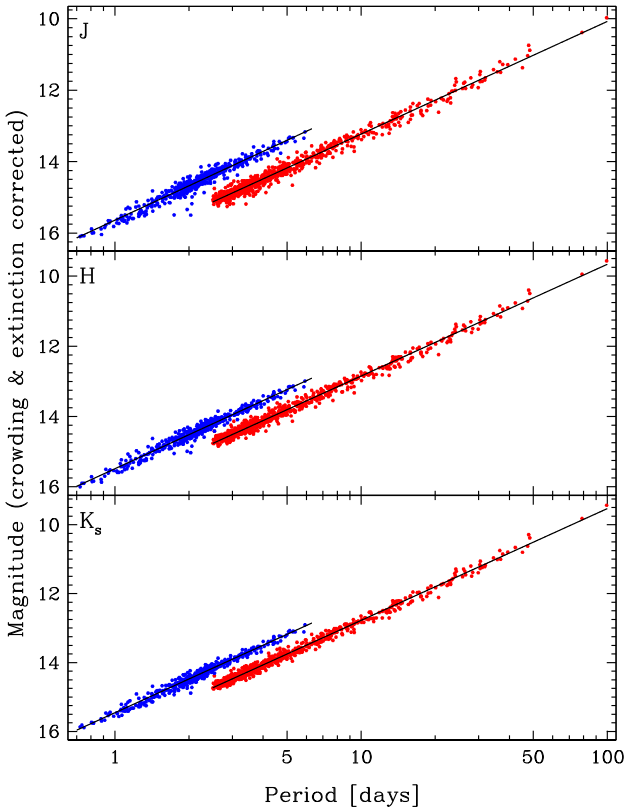

Figure 15. Final Leavitt Laws for FU and FO Cepheids, plotted using filled red and blue symbols, respectively.

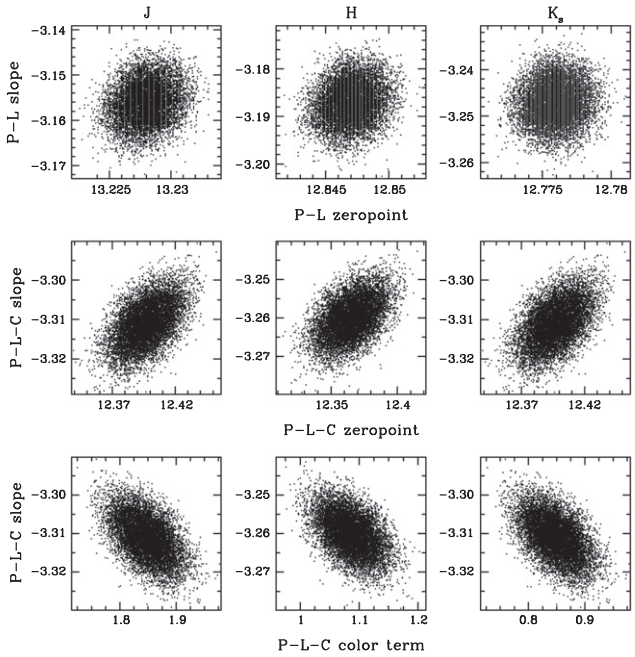

Figure 16. Result of 10^4 random realizations of the P-L and P-L-C fitting procedures for FU Cepheids, used to estimate the statistical uncertainty and correlation of the derived parameters. The limits of each panel span $\pm 4\sigma$ in the respective parameter.

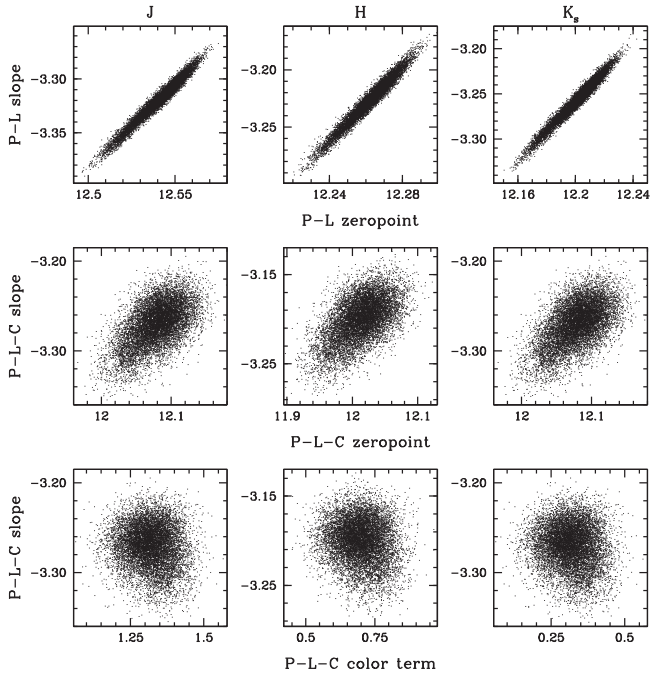

Figure 17. Result of 10^4 random realizations of the P-L and P-L-C fitting procedures for FO Cepheids, used to estimate the statistical uncertainty and correlation of the derived parameters. The limits of each panel span $\pm 4\sigma$ in the respective parameter.

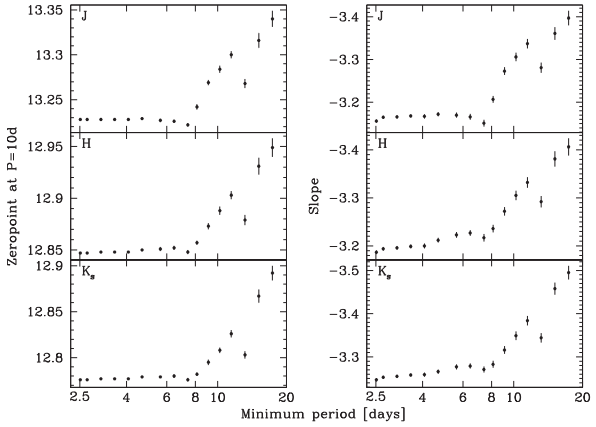

Figure 18. Changes in Leavitt Law parameters for FU Cepheids when restricting the sample by minimum period.